Testing the Full-Span High-Lift Common Research Model at the ONERA F1 Pressurized Low-Speed Wind Tunnel

Sylvain Mouton, Grégoire Charpentier, Annabelle Lorenski

Testing the Full-Span High-Lift Common Research Model at the ONERA F1 Pressurized Low-Speed Wind Tunnel

Sylvain Mouton[a1], Grégoire Charpentier[a2], and Annabelle Lorenski[b3]
[a]*ONERA, Le Fauga-Mauzac Test Center, 31410 Mauzac, France*
[b]*ONERA, 5 rue des Fortifications, CS 90013, 59045 Lille Cedex, France*

This paper presents the main features and outcomes of the wind tunnel testing of the High-Lift Common Research Model full-span model in the ONERA F1 pressurized low-speed wind tunnel. Two complementary test campaigns were carried out in 2022 and 2023, and included variation in model configurations, angle of attack, angle of sideslip, Mach and Reynolds numbers, and included force and moment, pressure, wing deformation, and flow visualization data. The main elements of the test methodology are reviewed to better appreciate the quality of the database, in terms of uncertainty, repeatability, and wall and support corrections. A selection of results is presented regarding longitudinal and lateral characteristics, the build-up of the landing configuration, Mach and Reynolds number effects, and flap setting effect. A special focus is accorded to data used in the fifth High-Lift Prediction Workshop.

Nomenclature

α	=	Angle of Attack, degrees
β	=	Angle of Sideslip, degrees
b	=	Model half span, $b = 1.50674$ m
c	=	Local chord of wing section, meters
C_X	=	Drag coefficient in wind axes
C_Y	=	Side force coefficient in wind axes
C_Z	=	Lift coefficient in wind axes
C_{LAA}	=	Rolling moment coefficient in wind axes
C_{MAA}	=	Pitching moment coefficient in wind axes
C_{NAA}	=	Yawing moment coefficient in wind axes
C_A	=	Axial force coefficient in body axes
C_{YA}	=	Side force coefficient in body axes
C_N	=	Normal force coefficient in body axes
C_{LA}	=	Rolling moment coefficient in body axes
C_{MA}	=	Pitching moment coefficient in body axes
C_{NA}	=	Yawing moment coefficient in body axes
C_p	=	Pressure coefficient
Δ	=	Difference between runs
δz	=	Vertical wing displacement at mid-chord, under wind loading, meters
$\delta\theta$	=	Aerodynamic twist of the wing, under wind loading, degrees
M	=	Mach number
Re	=	Reynolds number based on model reference length
p	=	Static pressure, Pascals
q	=	Dynamic pressure, Pascals
S_{ref}	=	Model reference surface, $S_{\text{ref}} = 1.00905$ m^2
L_{ref}	=	Model reference length, $L_{\text{ref}} = 0.35925$ m
X, Y, Z	=	Coordinates in tunnel reference frame, with origin at tunnel center, meters
x, y, z	=	Coordinates in model reference frame, meters

Subscripts

0	=	Indicates flow conditions at model location
i	=	Indicates stagnation conditions
c	=	Indicates data fully corrected from wall and support interference

I. Introduction

The continuous rise in computational power in the past decades has prompted the extensive use of Computational Fluid Dynamics (CFD) for the design and analysis of aerospace products. However, the extent to which it can be used to accurately predict aerodynamic characteristics of typical high-lift configurations of transport aircraft remains insufficient to fulfill industrial needs. This originates from limitations in the physical modelling and/or numerical discretization of phenomena such as flow separation or boundary layer transition [1]. Metrics that are important to the success and safety of the aircraft, such as the maximum lift coefficient, are therefore often improperly and inconsistently predicted by simulations, as exemplified in the previous AIAA High-Lift Prediction Workshops (HLPW) [2][3].

[1] Assistant Director for Scientific and Technical Development, Le Fauga-Mauzac Wind Tunnel Department.
[2] Test engineer, Le Fauga-Mauzac Wind Tunnel Department.
[3] Model designer, Engineering and Models Department.

As a consequence, the determination of aircraft high-lift performance strongly relies on wind tunnel testing, which also comes with some limitations, such as compromises in the geometrical modeling of the aircraft, or Reynolds number effects.

In order to advance both CFD and wind tunnel capabilities, a High-Lift Common Research Model (CRM-HL) ecosystem has been started to promote dialogue between computational and experimental researchers and practitioners [4]. This ecosystem benefited from a first high-lift configuration [5] based on the high-speed Common Research Model (CRM) shape [6][7]. This configuration was used to manufacture a 10% semi-span model that was first tested at the NASA Langley Research Center 14-by-22 foot atmospheric wind tunnel in late 2018 [8][9], then at the Qinetiq 5 m pressurized wind tunnel in 2019 [10], and again in the 14-by-22 foot tunnel in 2020/2021 for acoustics purpose [11]. Geometry and results from the test in the Qinetiq 5 m tunnel were used in the fourth HLPW (HLPW-4) [12], which also stimulated considerable computational efforts, e.g. [13]. This geometry was however limited by the mechanical capabilities of the 10% semi-span model, so that between 2020 and 2021, some further small improvements were brought to the configuration, to come up with the present "Initial reference configuration" [14], that is used in the fifth HLPW (HLPW-5). Based on this shape, a 1/19.5 (≈5.9%) full-span model was designed and manufactured at ONERA, and it was called LRM-HL for "Large Reference Model – High-Lift". This model and test is a follow-up of a broader effort from ONERA to participate in the CRM community, which already produced wind tunnel tests and flow simulations on the high-speed configuration [15][16][17][18]. This effort aims at the following objectives:

- to build an open experimental capability and database for the scientific community,
- to use the models as test benches for the development and demonstration of testing techniques,
- to enable comparisons across wind-tunnels,
- to be a long-term reference model for the wind-tunnels.

In many aspects, these goals were aligned with those exposed in [19] for the purpose of CFD validation, so that recommendations and requirements from [19] could be taken into account.

The present paper introduces the F1 wind tunnel (section II), the LRM-HL model (section III) and the experimental methodologies (section IV). It then presents some results of the test campaigns respectively carried out between March 29th and April 19th, 2022 and between February 2nd and February 15th , 2023 (section V). Most of the results presented are related to the test cases 2 and 3 selected in the HPLW-5. In that respect, this paper can be regarded as introducing the experimental dataset used as validation data in the workshop. Data sharing policy and availability are presented in section VI. This paper extends a previous AIAA publication [20], as it now presents and compares results from two test campaigns, and it reveals results that were previously presented unscaled. In order to avoid constantly referring the reader to this previous publication, some parts of it are repeated in the present paper.

II. Overview of the F1 low speed pressurized wind tunnel

Only a brief description of the ONERA F1 wind-tunnel is given here to provide some context of the experimental campaign carried out. The reader is referred to references [21] and [22] for a more complete description. The wind tunnel is of pressurized, closed-circuit type. The rectangular circuit is built of pre-stressed concrete, has an overall volume of some 13 000 m^3, and can be pressurized up to 3.85 bar. The settling chamber is 12 m in diameter and is fitted with a honeycomb filter and three turbulence screens. It is followed by a metallic convergent which ensures the passage to the rectangular test section, with a 7.2 contraction ratio. The test section is rectangular, 4.5 m wide, 3.5 m high and 11 m long. The side walls are slightly diverging to compensate for the growth of wall boundary layer and achieve negligible stream wise velocity gradient. The wind-tunnel motor is a 9.5 MW asynchronous electric motor, driving a fan of 7.4 m diameter at a constant speed of 360 RPM. The pitch angle of the 16 blades of the fan is controlled to adjust the tunnel speed. A heat exchanger in the return circuit maintains the air temperature in the tunnel to about 25°C to 30°C. To ensure a high productivity, the test section can be isolated from the rest of the circuit by two cylindrical sliding doors, which enables access to the model within 10 min after wind is turned off, while keeping the rest of the circuit pressurized. The test section itself is mounted on a cart that can be removed from the aerodynamic circuit to carry the whole model and testing apparatus from and to different preparation cells in order to optimize the run-up time of the tunnel.

A large number of model setups is available, for full-span models, half-span models, air inlets and propellers, using either internal or floor balance. The wind tunnel is used by worldwide customers to investigate the low-speed aerodynamics of aircraft, but also of air intakes (see e.g. [23]), under high-Reynolds conditions.

The tunnel flow quality was documented with the most recent knowledge in [24]. Across the volume occupied by the full-span models, the dynamic pressure is homogeneous within ±0.3% and the flow angle within ±0.15° of their mean values. The longitudinal turbulence intensity is lower than 0.08% and the noise intensity is lower than 0.05% (integrated in the 10 Hz – 5 kHz band) over most of the operating envelope of the tunnel (after [21] and more recent unpublished data).

Tunnel calibration procedure to determine flow conditions at model location from tunnel sensors was also explained in details in [24], along with the redundancy checks between the different sensors that are performed for each run.

III. Overview of the LRM-HL wind tunnel model

a. single-strut setup **b. three-strut setup**

Figure 1: LRM-HL model in F1 wind tunnel

A. Model shapes and configurations

As described in introduction, the LRM-HL is a 1/19.5 (≈5.9%) scale full-span model of the "Initial reference configuration" of the CRM-HL [14]. The model span is 3.02155 m and the fuselage length is 3.30063 m. All dimensions in this paper are provided at model scale, in S.I. unit. The origin of model axes, the position of the moment reference point, and the model reference length and surface are in agreement with the ones defined in the CRM ecosystem.

1. Clean wing LRM

This paper is mostly about the test of the high-lift model, however some results from the clean wing model will also be presented. The shape of the clean wing LRM corresponds to the high-speed wing shape of the CRM, as described in [7]. As explained in [5], this clean wing geometry is not identical to the CRM-HL wing with stowed high-lift devices. Most notably the high-lift wing has a larger leading edge radius on the slat, a constant dihedral angle and a different trailing edge thickness.

2. High-Lift LRM

This model shares the same fuselage and empennages than the clean wing model. The shapes, and especially the high-lift system and nacelles, have been described in [14]. CAD model of the wing have been shared within the CRM-HL ecosystem, and integrated into the design. However, this CAD model did not specify shape for the slat brackets, the flap brackets and the Flap Support Fairings (FSFs), only their number and spanwise position was available, completed by guidelines for their size and architecture given in [14]. Therefore, slat and flap brackets were designed for the present model, incorporating these pieces of information. The FSFs from HLPW-4 geometry were reused, only slightly adapted to cope with their new position. They were also broken down into an underwing fixed part and a moveable part, connected with a hinge line. Due to schedule issue, the final release of the Wing Under Slat Surface (WUSS) of the CRM-HL reference configuration could not be used for that model. This resulted in local deviation (0.6 mm), but only on the most outboard part of the wing. 2D simulations tend to indicate that this small deviation is expected not to change the flow physics or wing performance.

Table 1: Model configurations.

Conf. name	Short description	Relevant for HLPW-5 case #	Nacelle	Tail plane	Slat deflection (inboard / outboard)	Flap deflection (inboard / outboard)
T/O	Take-off	-	on	on	**22° / 22°**	**25° / 25°**
WBSHV	Slat only, no nacelle	2.2	**off**	on	30° / 30°	**0° / 0° (stowed)**
WBSFHV	Slat and flap, no nacelle	2.3	**off**	on	30° / 30°	40°/37°
LDG-HV	Full landing	2.4	on	on	30° / 30°	40°/37°
LDG	Full landing, no tail planes	3	on	**off**	30° / 30°	40°/37°
LDG−3	Landing −3°, no tail planes	-	on	**off**	30° / 30°	**37°/34°**
LDG+3	Landing +3°, no tail planes	-	on	**off**	30° / 30°	**43°/40°**

The high-lift devices can be set in take-off reference configuration (T/O) or landing reference configuration (LDG). Alternate landing configuration (LDG−3 and LDG+3) are also available. It is also possible to stow the flap into the wing to retrieve the shape of the trailing edge of the clean wing. The nacelles can be removed from the model, and a filler piece is then fitted to ensure continuity of the slat through the whole span, as was already done in [8]. The configuration reported in

the paper are described in Table 1. CAD files describing the model shape under various configurations are provided in [25][12].

B. Model design and manufacture

The model was produced by the ONERA model design and manufacturing department located in Lille. It was meant to be as accurate as possible. For example, the pressure tubes connected to pressure taps on the slats are routed inside the slat brackets, without any aerodynamic obstruction in the slat gap.

A geometrical inspection was performed on the model, with the help of a mobile 3D measuring arm (Faro® Quantum measurement system). 15 sections were checked on each of the high-lift wings, and all of the 5 wing configurations described in Table 1 were inspected. Deviations resulting from this inspection are listed in the Table 2. From these results, the model is considered highly accurate. For example, the maximum positioning error of slats and flaps, that has a direct effect on the gaps between the high-lift elements, is within 0.295 mm/236 mm = 0.13% of the wing mean aerodynamic chord.

Table 2: Main results from geometrical inspection of the model (first value reported is the maximum measured across all inspected sections and all wing configurations; second value, written pω, indicates the ω^{th} percentile).

		Wing main body	Slats	Flaps	HTP	VTP	Fuselage
Positioning error	Twist	0.062° p85: 0.017°	0.220°	0.060°	0.014°	0.006°	N/A
	Dihedral	0.023°	N/A	N/A	0.017°	0.005°	N/A
	Sweep	0.012°	N/A	N/A	0.006°	0.017°	N/A
	Translation w.r.t. wing main body	N/A	0.267 mm p97: 0.15mm	0.295 mm p85: 0.15 mm	N/A	N/A	N/A
Shape error	position < 10% chord	0.066 mm	0.108 mm p71: 0.075 mm	0.069 mm p95: 0.05 mm	0.062 mm	0.031 mm	0.255 mm p89: 0.15 mm
	position > 10% chord	0.146 mm p94: 0.05 mm					
Roughness arithmetic average Ra			0.31 µm		0.38µm	0.32µm	0.48µm

C. Model setup on single-strut (1M) in the wind tunnel

In the first wind tunnel campaign in year 2022, already reported in [20], the LRM-HL model was mounted on the single-strut setup, using a 6-component internal balance. The setup is visible in Figure 1a. The pitch movement is achieved by a carriage travelling on a cradle under the floor, so that the model rotates approximately around the tunnel center. The maximum range of pitch angle for this test was about −9° to +24°. Movement in azimuth is achieved thanks to a turntable also located under the floor, and the range of azimuth angle was ±30°. In the following, reference to this campaign will be labelled “1M”.

D. Model setup on three-strut (3M) in the wind tunnel

In year 2023, another wind tunnel campaign took place with the same model, mounted on the so-called three-strut support, using a floor balance. The setup is visible in Figure 1b. The pitch movement is achieved by extending and retracting the rear strut, which rotates the model around the tip of the front struts. These front struts are attached to the model wing by pivot points housed in special enlarged Flap Support Fairing. The maximum range of pitch angle for this test was about −6° to +22°, and no displacement is azimuth was performed. In the following, reference to this campaign will be labelled “3M”.

E. Model finish

Once assembled during the test preparation, the model surface is prepared for the aerodynamic test. This consists in ensuring proper sealing between model parts in spite of the inevitable assembly game, filling or taping the holes housing assembly screws and pins, cleaning up the model surface and applying the device tripping the transition of the boundary layer. The result of these operations is presented as pictures in Figure 2.

Figure 2: Details of the wind tunnel model in LDG configuration.

The boundary layer transition was tripped using so-called “cadcut” strips. Each strip is glued on the model surface and consists in a row of circular dots of 1.27 mm diameter, placed every 2.54 mm. The thickness of the dots for this test was 114 µm on the empennages, and 127 µm on the fuselage, wings and nacelles. This thickness was selected in order to be

comparable to the test in Qinetiq 5 m wind tunnel [12], once the difference in model scale is taken into account. The location of the transition trips is indicated in Figure 3, with all dimensions given at model scale. No tripping is applied on section of the wings where slats and flaps are present.

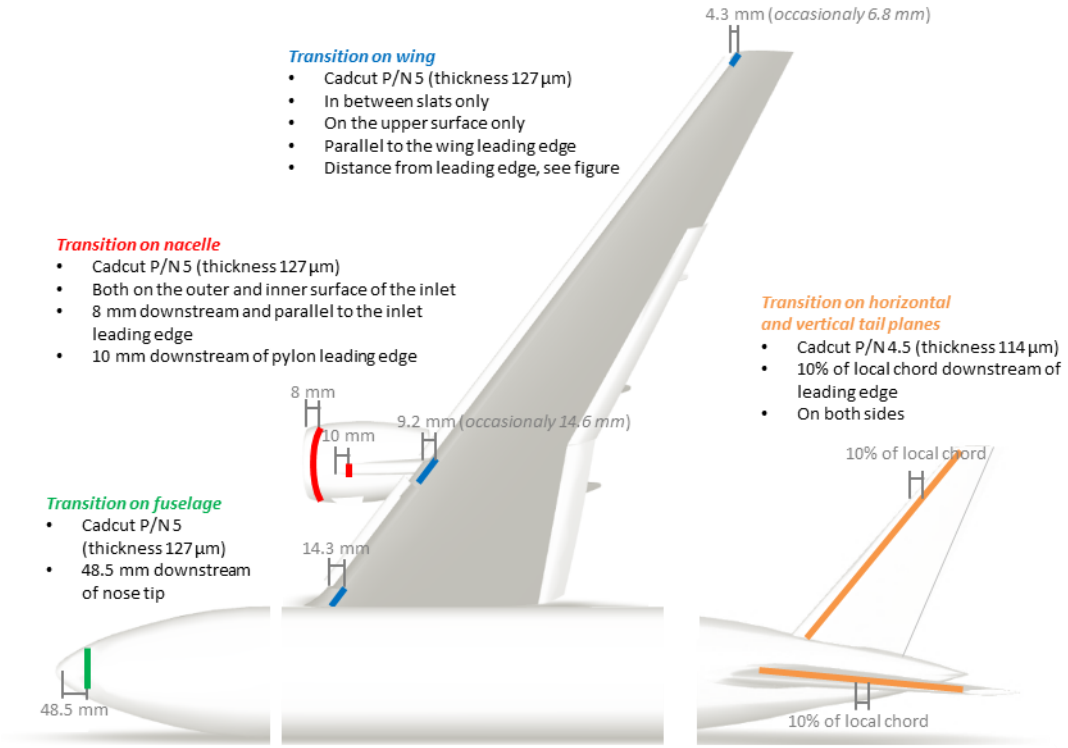

Figure 3: Details of the boundary layer transition.

Some variations to this nominal model finish were performed to observe the sensitivity of results:

1. transition on upper side of wings (blue lines in Figure 3) was moved aft (indicated in Figure 3 as "occasionally") to correspond to the configuration during previous tests with the 10% scale half-model [10], then it was completely removed;
2. the sealing in between flaps was reduced, with the length of the gap (distance from sealing to trailing edge, see Figure 2b) increased from 23 mm to 55 mm, again to better correspond to the configuration during previous tests [10].

Each variation was applied for only one run, after what the nominal finish previously described was used again.

IV. Test methodology

This section is illustrated with experimental results that were all obtained on the LDG conf, with tail planes, at a Mach number M_{0c} = 0.20 and a Reynolds number Re_{0c} = 5.9 million.

A. Sensors in the experiment

The main sensors involved in the experiment are presented in Table 3. The first part of the table lists the usual wind tunnel reference sensors that are used to determine the flow conditions in the test section. Using tunnel calibration laws, these reference sensors allow determining the flow conditions at model location in the wind tunnel, more especially total pressure, total temperature, and static pressure [24]. The second part of the table lists the main sensors dedicated to the present model and experiment. Some additional unlisted sensors are used to ensure in-situ calibration and monitoring of the pressure scanners. There also exist numerous sensors dedicated to the monitoring of the tunnel operation, but that are not used in the processing of the data reported in this paper. The column labelled "setup" indicates in which of the two test campaigns the sensors were installed.

Table 3: List of sensors in the experiment.

Sensor	Setup	Number and location	Quantity measured
Differential pressure sensor	both	6 behind wind tunnel walls (2.5 psi range)	Difference between reference total pressures and reference static pressures
Differential pressure sensor	both	2 behind wind tunnel walls (50 psi range)	Difference between reference total pressures and atmospheric pressure
Thermocouple	both	1 in settling chamber (type K)	Total temperature
Barometer	both	1 in instrumentation room	Local atmospheric pressure
Humidity sensor	both	1 in tunnel circuit	Moisture content of the air in the tunnel
Internal force balance PHI180 N°3	1M	1 inside the model fuselage	the 6 components of the force acting on the model
External force balance	3M	1 under the wind tunnel floor	the 6 components of the force acting on the model and exposed struts
Inclinometers	both	2 inside the model fuselage	pitch angle of the model
Angular potentiometer	both	1 under the floor	azimuth angle of the model
Electrical level	both	1 inside the model fuselage	horizontality of the model
Spirit level	1M	1 on top of model fuselage	horizontality of the model
Differential Electronic Pressure Scanners (ESP) PSI®	1M	8 inside the model fuselage (15 psi range) 3 under the floor (5 psi range) PSI® 8400 system in instrumentation bay	static pressure on model surface static pressure on wind tunnel walls
Strain gauges	both	3 half bridges in the right wing	Bending moment in the wing
Accelerometers	both	8 inside the model fuselage and wings	Model accelerations
Contact detection	1M	1 between strut and model	Absence of contact between metric and non-metric parts
Cameras for Model Deformation Measurement	1M	2 behind windows on the ceiling	Pictures of wing markers

449 static pressure measurements are distributed over the model and 115 on the wind-tunnel walls, as indicated in Table 4. The wing sections equipped with pressure taps are indicated in Figure 4.

Table 4: Static pressure taps on the model and wind-tunnel walls, during 1M setup

Part	Number of taps	Comments
Fuselage	48	including 12 near the strut
Vertical tail plane	27	over 1 section
Horizontal tail plane	81	over 3 sections, 2 on the left, 1 on the right
Wing	289	over 7 sections 3 on the left, 4 on the right, typically with 10 taps on the slat, 18 to 25 on the main body and 12 to 16 on the flap
Nacelle	4	Inside the right nacelle
Tunnel ceiling	45	over 3 rows
Tunnel left wall	35	over 3 rows
Tunnel right wall	35	over 3 rows
Total	564	

B. Continuous polars

During tests in F1, most of the runs are performed by continuously varying one of the test parameter and taking properly filtered and synchronized samples from the acquisition systems. In the present case, the AoA was varied at a rate of 0.3 degree/second (pitch-sweep run a.k.a. AoA-sweep run), and the Angle of Sideslip (AoS) at a rate of 0.5 degree/second (AoS-sweep run). Data stream for the forces and angles measurements is numerically filtered by a low-pass filter with a cutoff frequency of 1 Hz, and finally sampled at a rate of 2 points/second. With this setting, a pitch-sweep run with corrected AoA rising from about −9° to +23° is carried out in about 1 min 45 s and includes about 210 data points, one every 0.15°. Model pressure measurements are performed using a PSI® 8400 system, that scans the 10×64 different pressure ports at about 20 kHz, and returns the average of 6 samples, also at a rate of 2 points/second. The pneumatic tubing in between the pressure orifice and the sensor contributes to filter out the high frequency pressure fluctuations. Model deformation measurements are performed by cameras at rate of 1 point/second, unfiltered. The delays introduced by the different measurement systems are accounted for, so that data points are properly synchronized.

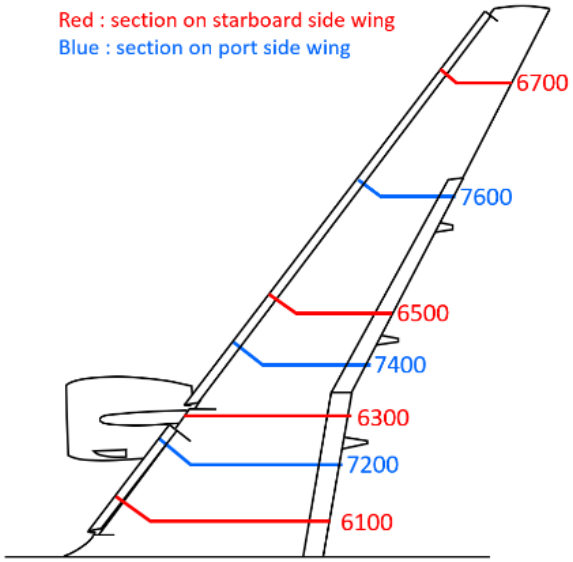

Figure 4: Position of wing sections equipped with pressure taps.

Figure 5 shows a comparison of data obtained during a continuous pitch-sweep run and data acquired under the same conditions but with a non-moving model (pitch-pause runs). Pitch-pause runs were carried out with the same acquisition rate and characteristics, over a duration of 60 s, i.e. 120 samples. All samples are shown in Figure 5 even if they visually collapse to single points, except past stall (in purple), which shows the scatter due to flow unsteadiness and model movements. The Figure 6 displays the same data plotted as differences in force coefficients between pitch-sweep and pitch-pause runs. These differences are mostly below 0.01 in lift, 10×10^{-4} in drag and 5×10^{-3} in pitching moment coefficients, which is less than the uncertainty to be exposed in section IV.F. Only past stall does the scatter considerably increase, as previously mentioned, but the average of the samples stays within the limits of the plot, with a difference in averaged lift coefficient of only 0.03 between pitch-sweep and pitch-pause runs. These results demonstrate that data filtering performed during continuous pitch-sweep runs was adequate to reject the high-frequency content in the signal, mostly introduced by the model and strut moving around their first eigenmode around 5 Hz, and to preserve only the quasi-steady aerodynamic forces in the low frequency range.

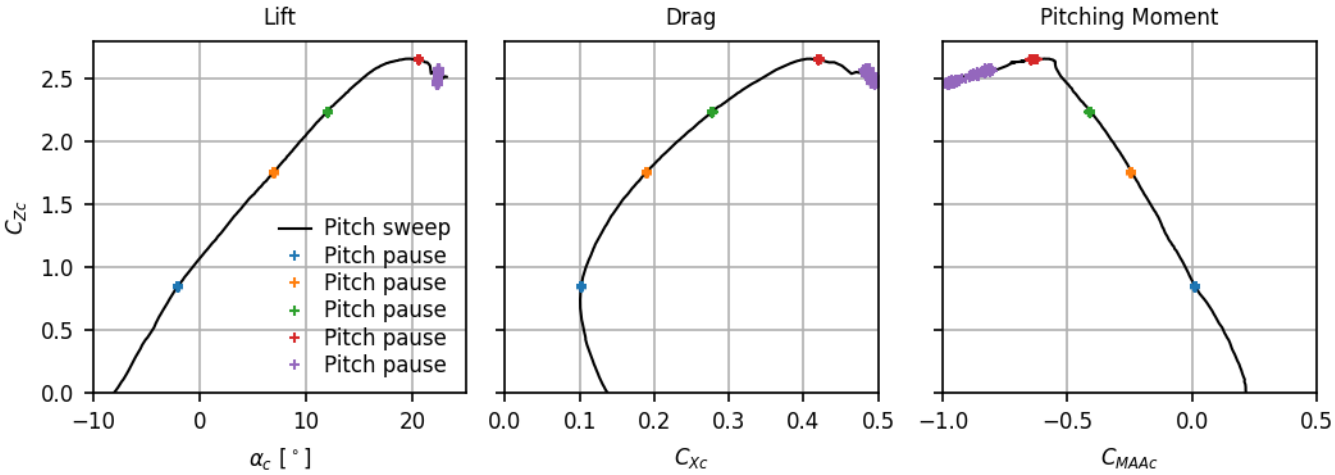

Figure 5: Comparison of force coefficients obtained during pitch-sweep and pitch-pause acquisition (runs 1387, 1407, 1408, 1409, 1410, 1411).

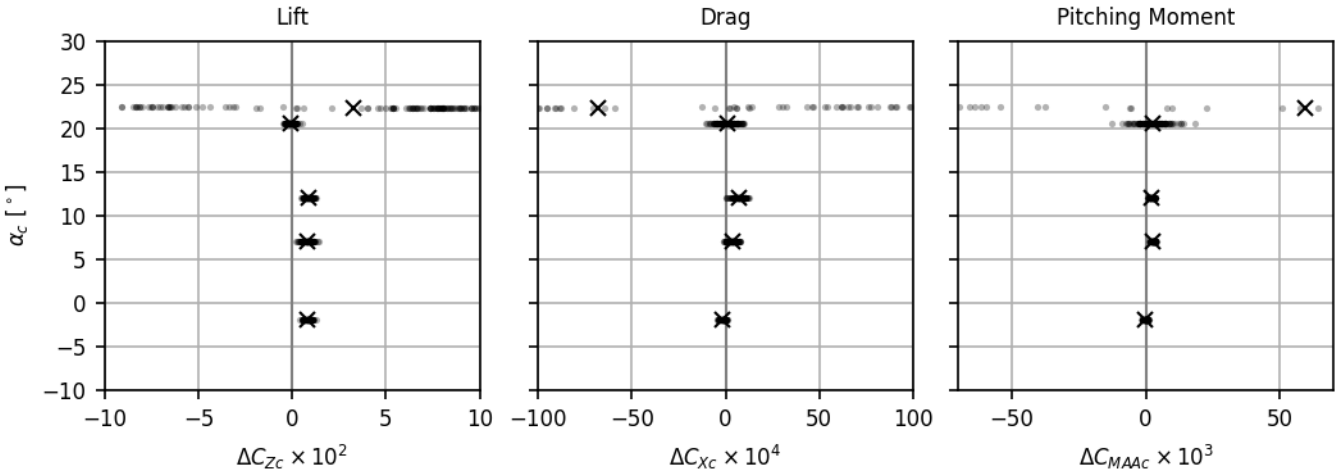

Figure 6: Difference in force coefficients between pitch-pause and pitch-sweep acquisition; each grey dot is a pitch-pause data point, and their average is shown as a cross (runs 1387, 1407, 1408, 1409, 1410, 1411).

To prove the good synchronization between the pressure measurements carried out with ESP and the rest of the data, we now examine the difference in pressure coefficient measured between one of the pitch-pause runs (the one near maximum lift, in red in Figure 5) and the same data measured during pitch-sweep runs. During these runs, there were 429 pressure taps out of 449 active on the model (95.5%), because the remaining taps had been detected as leaking or clamped during pre-run check. Hence the comparison between pitch-sweep and pitch-pause runs results in 429 differences in pressure coefficient, which are presented as a histogram in Figure 7.

It can be observed that the difference is within ±0.02 for 95% the taps, which is in agreement with the uncertainty to be exposed in section IV.F. Only 9 outliers exhibited $|\Delta C_p| > 0.05$. Further examination revealed that these outliers are located in regions strongly influenced by separated or vortical flow (e.g. downstream of the nacelle) that exhibit strong pressure fluctuations that were not completely eliminated by the pneumatic and electronic filtering during the pitch-sweep runs.

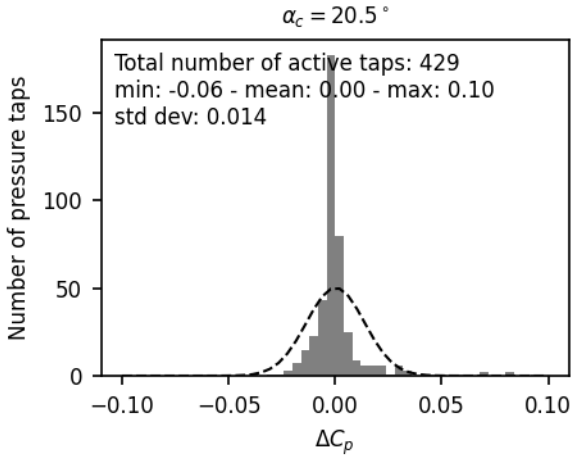

Figure 7: Histogram of differences in pressure coefficients between pitch-sweep (run 1387) and pitch-pause (run 1410) acquisition, near maximum lift (red cross in Figure 5). The dashed line is a Gaussian distribution having the same mean and standard deviation.

C. Wall corrections

In ONERA wind tunnels, the modeling of wall interference is based on linearized potential theory [26]. The aircraft model is represented by a set of point singularities, distributed over the fuselage, wing and horizontal tail plane. The position and intensity of each singularity is computed based on geometrical properties of the model (e.g. local chord, local cross-section), but also on actual measurements (lift and drag). In the case of F1, the boundary condition imposed by the solid rectangular walls could easily be solved by the method of images, but in fact the software uses Fourier transforms in order to be also able to cope with the porous walls encountered in transonic wind-tunnels. This modeling can output the complete three-dimensional wall-induced interference flow-field. This flow-field is then space-averaged along the span of the wing and empennage to come up with corrections in flow velocity and angle (known as first-order corrections [27] or primary

corrections [28]). The spatial variation in the wall-induced flow-field is then taken into account with complementary corrections of axial force and pitching moment angle (known as second-order corrections [27] or residual variations [28]).

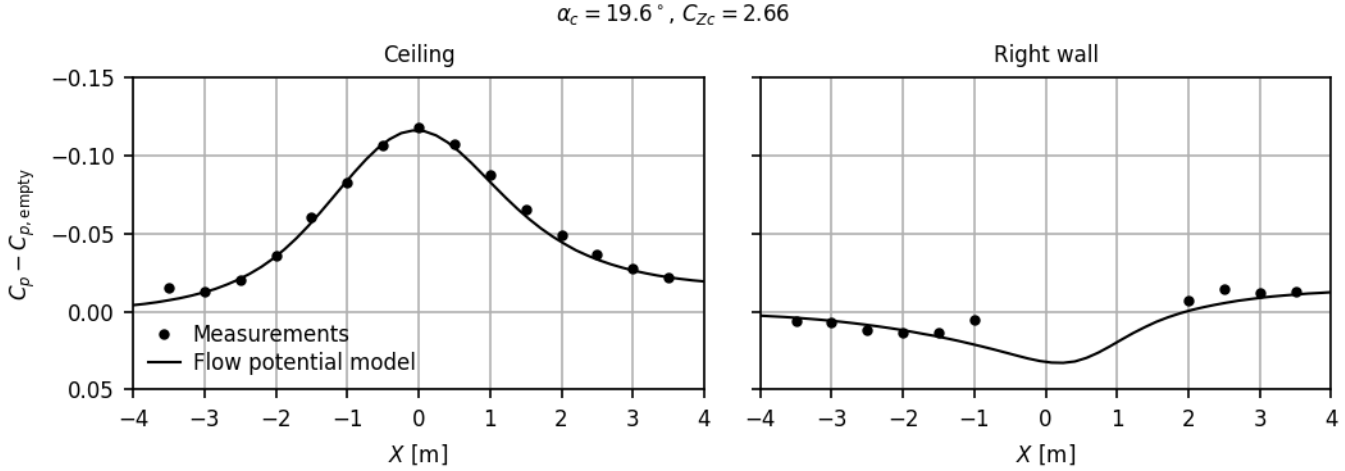

Figure 8: Pressure coefficient on wind tunnel walls, at maximum lift coefficient (run 22625/1387).

The validity of this set of corrections has been verified over the years by comparing results across wind tunnels (e.g. [29], [30]), with flight tests (e.g. [31]), and more recently with more advanced flow modelling (e.g. [27]). Additionally, it is possible to compare the pressure on the wind-tunnel walls predicted by the linearized potential model, with the pressure actually measured during the test. This is the purpose of the Figure 8. To obtain this figure, pressure coefficients measured during the empty tunnel calibration $C_{p,\mathrm{empty}}$ were subtracted from the pressure coefficients of the present campaign C_p, as recommended in [28], §8.3.2. Because the flow potential model is used to derive wall corrections only, it usually does not include the single-strut support. The effect of the support is accounted for in the support corrections described in the next section. However, to produce the plot of Figure 8, a flow potential model of the support was included in the modeling, mostly to represent the blockage effect of the support wake. The area without measurements for -1 m $< X <$ 2 m originates from the large glass windows installed on the tunnel side walls and visible in Figure 1. As mentioned in [28], the signal to measure is small and it is difficult to maintain high quality pressure tap orifices on the walls of a large wind tunnel, so that a couple of taps exhibit small inconsistencies (±0.015 in pressure coefficient). However, the overall agreement with the flow potential model is good. It validates the wall correction method by showing that the model description by means of discrete singularities is successful, and that, therefore, the wall-induced interference flow-field is also properly simulated.

D. Support corrections

In the previous publication [20], the support corrections for this experimental setup were derived from a previous wind tunnel test involving the clean wing version of the LRM model, which shares the same fuselage and support systems. During this experiment, a dummy strut was attached to the non-metric part of the setup, see figure 13 in [20]. This dummy strut was then removed to observe the effect on force coefficients. Like in the case of wall corrections exposed above, this effect was broken down between first-order corrections on flow velocity and angle, that are independent of the aircraft configuration and explain a large part of the support effect, and second-order corrections on axial force and pitching moment. Previous experience [32] indicated that this second-order correction mostly impacts the fuselage and tail plane so that results obtained on the clean wing configuration were used to process the high-lift configuration as well.

This assumption was verified by using the experimental setups depicted in Figure 9. During the single-strut campaign, a dummy three-strut support can be mounted on the wind tunnel floor (Figure 9b). Interference effect on forces is then measured using the model internal balance. Additionally, the effect of replacing the regular FSFs by the special FSFs housing the pivot point of the three-strut support was also investigated, and it was found insignificant. During the three-strut campaign, a dummy single strut can be mounted below the model (Figure 9a). This dummy strut is mounted on an internal balance (in fact the same one as was used during single-strut campaign), so that it moves with the model, and the aerodynamic forces on the dummy support can be subtracted from the readings of the floor balance.

Although not strictly speaking a support interference, the aerodynamic forces on the exposed parts of the struts during three-strut campaign (sometimes called “tare” forces) are measured using the floor balance during a short preliminary entry without the model mounted, as a function of Mach number, Reynolds number and vertical extension of the rear strut. These forces are then subtracted during the three-strut campaign. During runs with the dummy single strut, the rear strut stands in the wake of the dummy strut, which slightly changes the drag tare, and this is taken into account.

a. Setup for single strut interference **b. Setup for three strut interference**

Figure 9: Experimental setup for strut interference test.

To conclude about corrections, it is worth underlining that previous HLPW have relied on half-model testing for which no half-model mounting correction is applied, and no generally agreed correction technique is available to the authors' knowledge. The need for corrections in that case arises because the model is lying in the boundary layer that develops on the tunnel floor. In spite of the "peniche" often used to offset the model from the floor, this boundary layer strongly interacts with the model. Around the model, the boundary layer thickness varies as it responds to the local pressure field. Close to the fuselage, the boundary layer separates and rolls into a horseshoe vortex. The floor is therefore far from a perfect mirror plane as it would be in an inviscid flow modeling [33]. This has consequences at least on the flow on the inboard wing, as largely exemplified in [10], but may also impact the overall flow as the effective aspect ratio of the model becomes questionable due to the peniche height, which has direct consequence on the wing downwash and induced drag [34]. For these reasons, the authors believe that half models are well suited to some kinds of test, such as optimization of high-lift configuration, or jet effects with a powered model, but are not best suited to CFD validation.

E. Model deformation measurement

Wing deformation was measured during most of the 1M test campaign. Stereovision technique described in [35] was used for that purpose, using the markers visible in Figure 2, distributed over 14 wing sections. Raw marker displacements are transformed into vertical displacement and twist of each section. Additionally, for each data point, measurements were interpolated as a function of spanwise position using smoothing splines, with a tolerance of 1 mm for displacement, and 0.1° for twist, and enforcing clamping at wing root.

F. Measurement uncertainty

A detailed discussion on uncertainty is not the purpose of this paper. This section will therefore only provide the driving causes and the order of magnitude of the uncertainty in the present test. Uncertainty is regarded as Gaussian and is here provided as two sigma (95%) confidence intervals.

1. Uncertainty on forces with internal balance

The uncertainty of balance reading is estimated to be 10^{-3} of its measurement capacity on each component. This yields the Table 5 for the contribution of the balance to uncertainty on aerodynamic coefficients in body axes.

Table 5: Internal balance capacity and corresponding 2-σ uncertainty on force coefficients at 10 kPa dynamic pressure.

Component	Axial force	Side force	Normal force	Rolling moment	Pitching moment	Yawing moment
Measurement capacity	±8 310 N	±29 540 N	±92 210 N	±10 240 Nm	±15 140 Nm	±3 920 Nm
Uncertainty on aero. coef	$\pm 8\times10^{-4}$	$\pm 3\times10^{-3}$	$\pm 9\times10^{-3}$	$\pm 3\times10^{-3}$	$\pm 4\times10^{-3}$	$\pm 1\times10^{-3}$

2. Uncertainty on forces with floor balance

The uncertainty of balance reading is here estimated to be 10^{-3} of its calibration range on each component. Due to its architecture, the balance capacity is much larger and not representative of the uncertainty. Contrary to the internal balance, the floor balance is approximately aligned with the aerodynamic axes, so that the corresponding uncertainty in force coefficient is indicated in wind axes in Table 6. Also, as explained in section IV.D, this balance is used twice to produce

model aerodynamic coefficients: once for the tare of the three-strut support, and once for the actual test with the model mounted. For this reason, and assuming uncorrelated errors because the forces to measure are very different, and these two measurements may be carried out some time apart, the resulting uncertainty is augmented by a factor of $\sqrt{2}$. This yields the Table 5 for the contribution of the floor balance to the uncertainty on aerodynamic coefficients in aerodynamic axes.

Table 6: Floor balance calibration range and corresponding 2-σ uncertainty on force coefficients at 10 kPa dynamic pressure.

Component	Drag force	Side force	Lift force	Rolling moment	Pitching moment	Yawing moment
Calibration range	±9 800 N	±39 200 N	±49 000 N	±52 900 Nm	±35 300 Nm	±24 500 Nm
Uncertainty on aero. coef	$\pm 14\times10^{-4}$	$\pm 5.5\times10^{-3}$	$\pm 6.9\times10^{-3}$	$\pm 21\times10^{-3}$	$\pm 14\times10^{-3}$	$\pm 9.6\times10^{-3}$

3. Uncertainty on dynamic pressure

The key measurement to determine the dynamic pressure q_0, and therefore a key contributor to its uncertainty, is the measurement of differential pressure $p_{i0} - p_0$ between total and static pressure. As explained in [24], this is not directly measurable during the test. Instead, the differential pressure between a reference total pressure in the settling chamber and a reference static pressure near the entry of the test section is measured instead. Calibration laws, determined during empty tunnel calibration, are then used in order to deduce p_{i0}, $p_{i0} - p_0$, and finally q_0 in the test section. Actually, this differential pressure measurement is carried out by 6 redundant sensors (of 3 different types) of 2.5 psi capacity, independently connected to 6 different static pressure taps and 3 total pressure taps. In the present test, the sensor connected to the reference tap "C18" was used as the primary source of data. This gives the opportunity to compare each of the 5 other measurements, to experimentally evaluate the uncertainty on $p_{i0} - p_0$, which is itself almost equal to the uncertainty on dynamic pressure q_0. Examination of Figure 10 reveals that this uncertainty if of the order of 35 Pa (two sigma value) at the highest dynamic pressure, and reduces to 15 Pa at the lower end of dynamic pressure range, which allows to derive Table 7. These observed values are consistent with the statements in the datasheets of the sensors and measurement hardware. The corresponding uncertainty on velocity, Mach number and Reynolds number is negligible for subsonic testing.

Table 7: 2-σ uncertainty on dynamic pressure.

Dynamic pressure	q_0 = 2 kPa	q_0 = 14 kPa
Uncertainty on dynamic pressure	±15 Pa	±35 Pa
Relative uncertainty on dynamic pressure	±0.75%	±0.25%

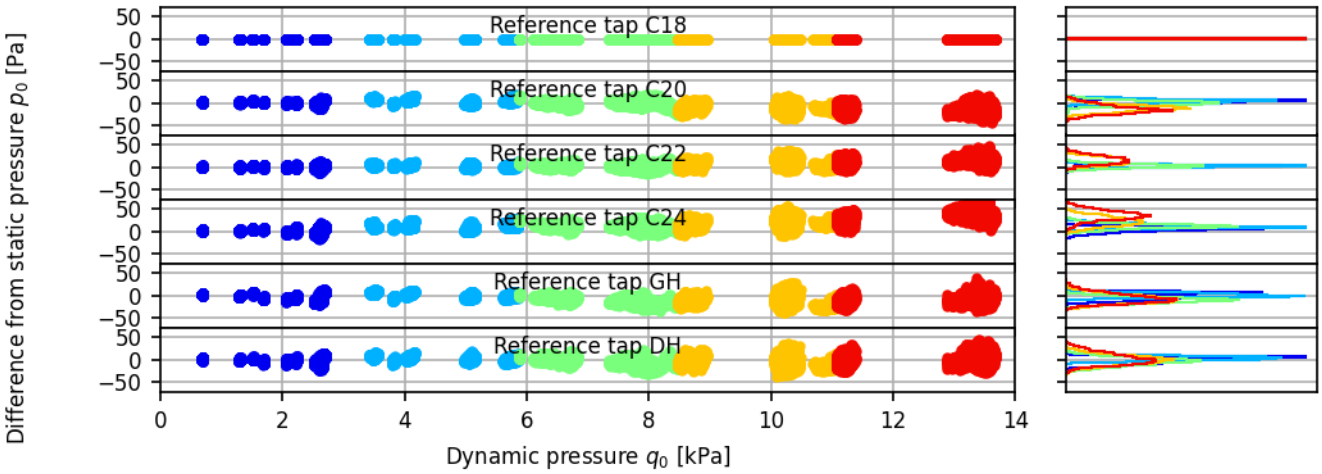

Figure 10: Comparison of readings from redundant sensors for the determination of tunnel static pressure p_0 (all runs of test campaign on single-strut, tap C18 used as reference; points are grouped into 5 ranges of dynamic pressure, corresponding to the 5 colors, to plot histograms on the right).

4. Uncertainty on angle of attack

Limiting ourselves to zero-sideslip runs, the Angle of Attack (AoA) is the sum of model pitch angle and tunnel upwash. From sensor datasheet, the uncertainty on model pitch angle measurement is below 0.01°, and it can be confirmed by comparing the two redundant sensors placed in the model. The uncertainty on tunnel upwash is estimated to be ±0.02° [24]. Total uncertainty is then about 0.022°, for both campaigns.

5. Combined uncertainty on uncorrected lift, drag and pitching moment

Uncertainty on force coefficients can be obtained by propagating the above sources into the calculations, assuming statistically independent errors. Table 8 shows examples of typical result for a case at Mach 0.20 and a total pressure of 3.82 bar, which yields a dynamic pressure of 10 kPa and a Reynolds number of 5.9 million.

Table 8: Example of typical 2-σ uncertainty on uncorrected longitudinal force coefficients for a dynamic pressure of 10 kPa.

		single-strut campaign		three-strut campaign	
Parameter	Value	Uncertainty	Relative uncertainty	Uncertainty	Relative uncertainty
AoA	15°	±0.022°	±0.2%	±0.022°	±0.2%
Lift	2	±0.011	±0.5%	±0.009	±0.4%
Drag	0.20	±0.0027	±1.3%	±0.0017	±0.8%
Pitching moment	−0.30	±0.0017	±0.6%	±0.0050	±1.7%

6. Combined uncertainty on corrected lift, drag and pitching moment

Values in Table 8 apply to uncorrected data. Correcting for the wall (sections IV.C) and support (section IV.D) interference effects introduces additional uncertainties that are more difficult to quantify.

With the experimental method used to correct for support interference, final corrected force coefficients actually rely on three different measurements, which can conceptually be written as : "corrected = uncorrected − (dummy strut on – dummy strut off)". If errors were uncorrelated across these three measurements, the uncertainty on corrected force coefficients would be about $\sqrt{3} \approx 1.7$ times those of the uncorrected ones (provided in Table 8). It is regarded as a worst case scenario, since the same balance measuring about the same forces is involved, over a short period of time, so that some correlated errors will cancel out in the difference "dummy strut on – dummy strut off". Also, the support interference effect is described with the help of a regressive law, which smooths out some of the random errors. A better indication of the uncertainty associated with support corrections may be estimated by considering the RMS of residuals of the regression, all model configurations and flow conditions included, provided in Table 9.

Table 9: RMS of residual of regression law for support correction

	single-strut interference		three-strut interference	
	no HTP	with HTP	no HTP	with HTP
Normal force	0.009	0.012	0.004	0.005
Axial force	0.0017	0.0018	0.0008	0.0008
Pitching moment	0.005	0.008	0.003	0.005

Uncertainty associated with wall corrections are epistemic, as they result from the modeling of the real flow using potential flow theory and how different parts of the model will react to the interference flow field. Evaluation of this uncertainty was not considered in the present work, and it is taken to be zero.

Table 10 is obtained by adding and propagating support correction uncertainties.

Table 10: Example of typical 2-σ uncertainty on corrected longitudinal force coefficients for a dynamic pressure of 10 kPa.

		single-strut campaign		three-strut campaign	
Parameter	Value	Uncertainty	Relative uncertainty	Uncertainty	Relative uncertainty
AoA	15°	±0.022°	±0.2%	±0.022°	±0.2%
Lift	2	±0.014	±0.7%	±0.010	±0.5%
Drag	0.20	±0.0032	±1.6%	±0.0019	±0.9%
Pitching moment	−0.30	±0.0053	±1.8%	±0.0059	±2.0%

It seems worth underlining that some of the uncertain errors previously discuss are not random across runs (for example tunnel upwash) and therefore are not evidenced by repeat runs. In general, a good repeatability is a necessary but not a sufficient condition for accuracy. This matter of fact is fortunate for the tests that seek to identify increments in between different runs, such as during configuration optimization. In the present case however, with the present dataset strongly tied to CFD validation, a full evaluation of uncertainty was deemed appropriate.

7. Uncertainty on model pressure coefficients

The uncertainty on uncorrected model pressure coefficient $C_p = (p - p_0)/q_0$ originates from the measurement of the differential pressure $p - p_0$ on one side, that implies the Electronic Pressure Scanners (ESP) plus another differential pressure sensor; and the measurement of the dynamic pressure q_0 on the other side (see IV.F.2). As a result, the uncertainty is dependent on the flow conditions. Some examples are provided in the Table 11.

Table 11: 2-σ uncertainty on uncorrected pressure coefficient.

Pressure coefficient	q_0 = 2 kPa	q_0 = 14 kPa
C_p = 0	±0.08	±0.01
C_p = −10	±0.11	±0.03

The uncertainty on corrected model pressure coefficient $C_{pc} = (p - p_{0c})/q_{0c}$ should incorporate the uncertainty on the velocity correction because it impacts corrected static and dynamic pressure p_{0c} and q_{0c}.

G. Measurement repeatability

1. Short and medium term repeatability during single-strut campaign

In F1 wind-tunnel, the short-term repeatability is always verified by performing a down-sweep polar immediately after each up-sweep polar. This allows immediately identifying any drift or hysteresis in the measurement process, but also sometimes small model deterioration, such as a piece of adhesive tape being peeled off the surface. The result of this comparison is shown in Figure 11, for a run in LDG-HV configuration, at Mach 0.20 and a Reynolds number of 5.9 million. At this plot scale, the only difference that can be spotted is a classical hysteresis effect past stall. Interestingly, this configuration presents with a limited amount of hysteresis that manifests itself only about 2° beyond maximum lift.

The black curve in Figure 12 shows the same data presented as differences in force coefficient at iso-AoA between up- and down-sweep runs. The magnitude of these differences is comparable to the scatter observed in Figure 6 and representative of the uncertainty exposed in section IV.F and plotted as error bars. The larger difference at high AoA, past maximum lift, is related to the hysteresis effect, mentioned above.

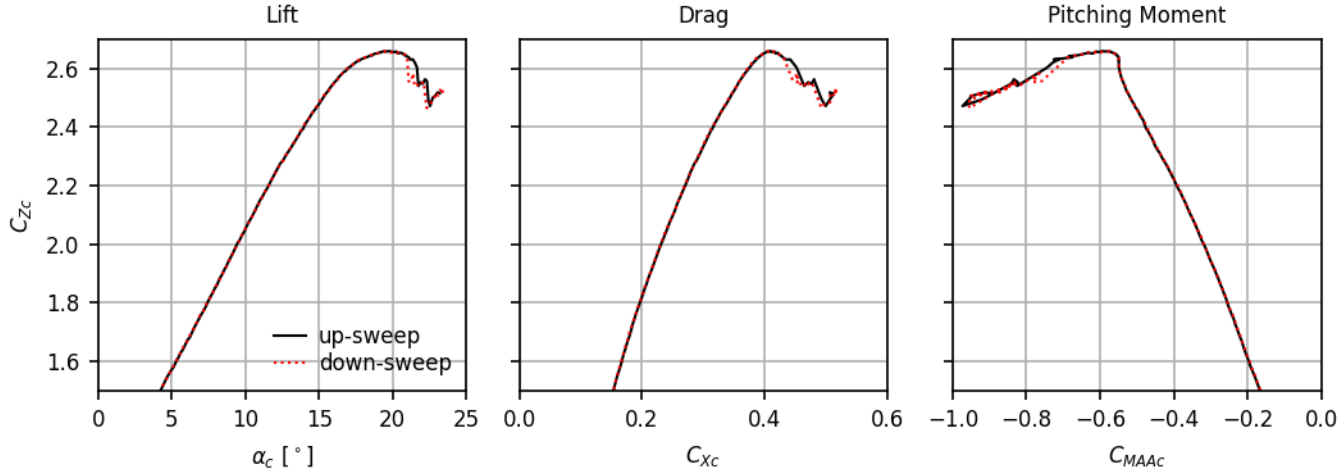

Figure 11: Force coefficients during 1M campaign, during up-sweep (run 22625/1387) and a down-sweep (run 22625/1388) runs, on LDG-HV configuration, at Mach number M_{0c} = 0.20 and Reynolds number Re_{0c} = 5.9 million.

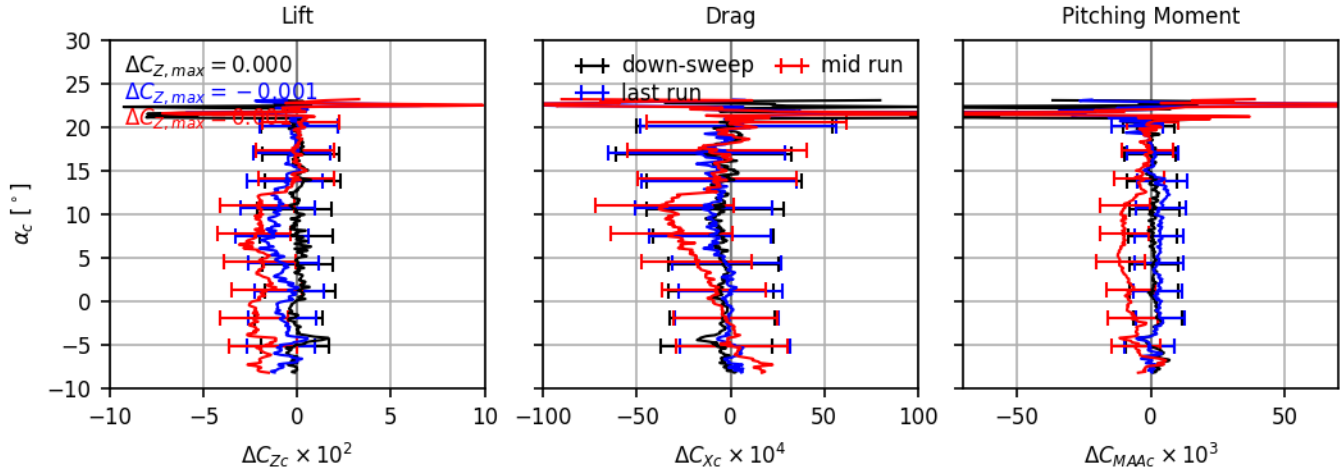

Figure 12: Differences at iso-AoA in force coefficients during 1M campaign, on LDG-HV configuration, at Mach number M_{0c} = 0.20 and Reynolds number Re_{0c} = 5.9 million. Reference run is the first up-sweep run of the test

campaign (run 22625/1387); differences are plotted for the down-sweep run immediately following (run 22625/1388, black lines), the last run of the test campaign (run 22639/1788, blue lines), and a run in between (run 22634/1659, red lines). Error bars results from the uncertainty model exposed in section IV.F.

More interesting is the mid-term repeatability also shown in Figure 12, also for the LDG-HV configuration, in blue and red lines. At first, the blue lines plot the differences in force coefficients between the last run of the test campaign (run 1788) and the first one (run 1387). In between these two runs, 14 tunnel rotations have elapsed, the tufts have been set and removed on the right wing, oil flow visualization has been performed twice on the right wing, the nacelles were removed and put back again, and the flaps have been stowed (for the component build-up investigation reported in section V.A), then set back into LDG configuration, which implied reapplying the sealing and tape on all the flaps and flap track fairings. The repeatability was almost as good as in the short-term, below 0.02 in lift, 15×10^{-4} in drag and 5×10^{-3} in pitching moment coefficients, again in agreement with the uncertainty estimations.

In between runs 1387 & 1788, some other repeats were regularly performed (runs 1594, 1614, 1617 and 1659). They sometimes showed less lift (−0.01 to −0.04 for a given AoA) and more nose down moment (−0.010 to −0.020 for a given lift coefficient) at $\alpha_c \lesssim 15°$, as represented by the red lines in Figure 12. After examination of lateral forces and pressure measurements, this could be traced to a physical phenomenon occurring on the inner right flap that caused the inboard right wing sections to produce slightly less lift than the left sections. Although this phenomenon was measurable, its magnitude was deemed sufficiently small not to deserve further investigation, but it points out that the flow on the inner flap at low AoA is very sensitive to small details of the configuration. At higher AoAs $\alpha_c \gtrsim 15°$, repeatability was very good throughout the whole campaign, and the maximum lift coefficient was repeated to better than 0.005 for the LDG configuration, at Mach 0.20 and a Reynolds number of 5.9 million.

2. Long term repeatability across different campaigns

Long term repeatability will be examined in section V.A.2, when comparing results across the two different campaigns reported in this paper.

H. Oil flow visualization

Some oil flow visualizations were carried out on the right wing, mostly during the three-strut test campaign. The model was painted with a mixture of mineral oil and colored pigments, using different colors on different parts of the wing. For runs performed during the three-strut campaigns, the lower surface of the wing and the nacelle were painted in blue, whereas the upper surface was painted in green. With such a setup, flow separation reaching the trailing edge is evidenced by blue paint being entrained towards the upper surface.

The model is then exposed to the air flow at desired conditions for a few minutes. Photographs are taken during and after the run under UV illumination. For each run, an overview picture is taken immediately after wind off by a remote-controlled camera located behind a window of the ceiling. Then, some additional close-up pictures are taken using a hand-held camera about 10 minutes after wind off, the time necessary to access the model when the tunnel is pressurized. The oil pattern does not change during this delay, except sometimes in place of large recirculation where some oil can be trapped and tends to flow down under the effect of gravity once the wind is turned off. Note also that adhesive tape was applied to protect the pressure taps from oil pollution, and this tape is visible on the pictures because it weakly glows under UV light. Although it is somewhat distractive in picture interpretation, closer examination reveals that the tape is not perturbing the flow.

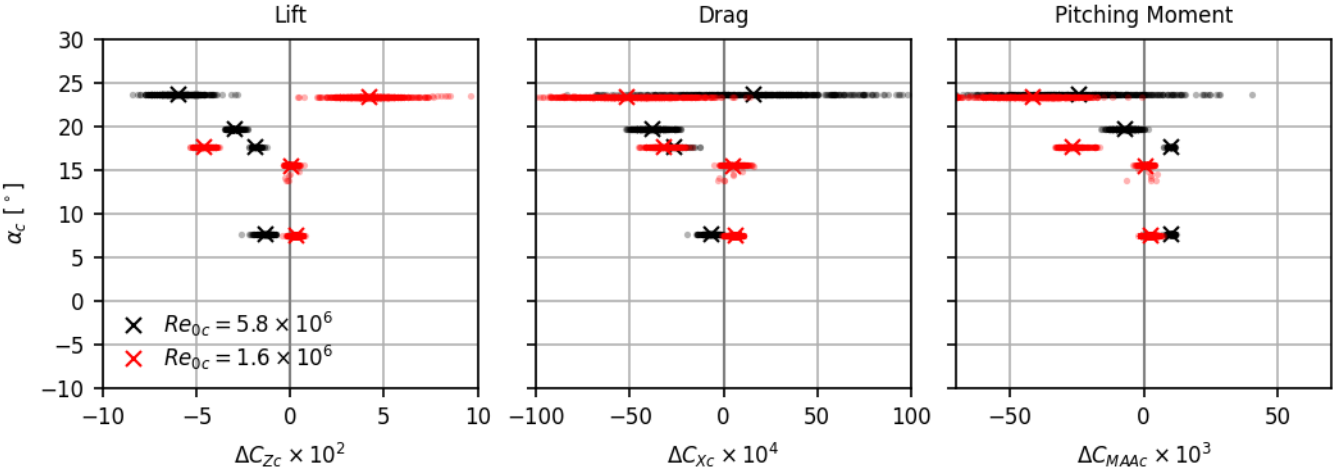

Figure 13: Difference in force coefficients during 3M campaign, between runs with oil flow on right wing (runs 22720/1377, 22721/1386, 22722/1395, 22723/1404 at Re_{0c} = 5.9 million) and run without oil flow (run 22713/1299 at Re_{0c} = 5.9 million), on LDG-HV configuration, at Mach number M_{0c} = 0.20 and Reynolds number.

The Figure 13 shows the effect of applying oil onto the right wing. The oil generally entails a penalty in lift comprised between 0.01 and 0.05, especially close to maximum lift ($17° \leq \alpha_c \leq 20°$). Examination of rolling moment confirms that the lift reduction indeed occurred on the right wing. Hence, if both wings had been painted, the lift coefficient would have been reduced by 0.02 to 0.10, which is significant. Therefore, oil flow is a good indication of the flow physics occurring on the wing, but it comes at the cost of some intrusivity. We may speculate that this may have been reduced if the leading edges of the different lifting element would not have been painted.

I. Tuft visualization

Tuft visualization was carried out on the left wing of the model throughout the entire 3M campaign. The tufts are polyamide threads, 0.16 mm in diameter and 20 mm in length. For each run, the tuft movements are observed using a camera recording at 25 images per second. UV illumination is used to make the tufts glow in the dark, and improve their visibility on the images in spite of their small size. Separated areas show up as regions were the tufts images are blurry and no longer oriented streamwise.

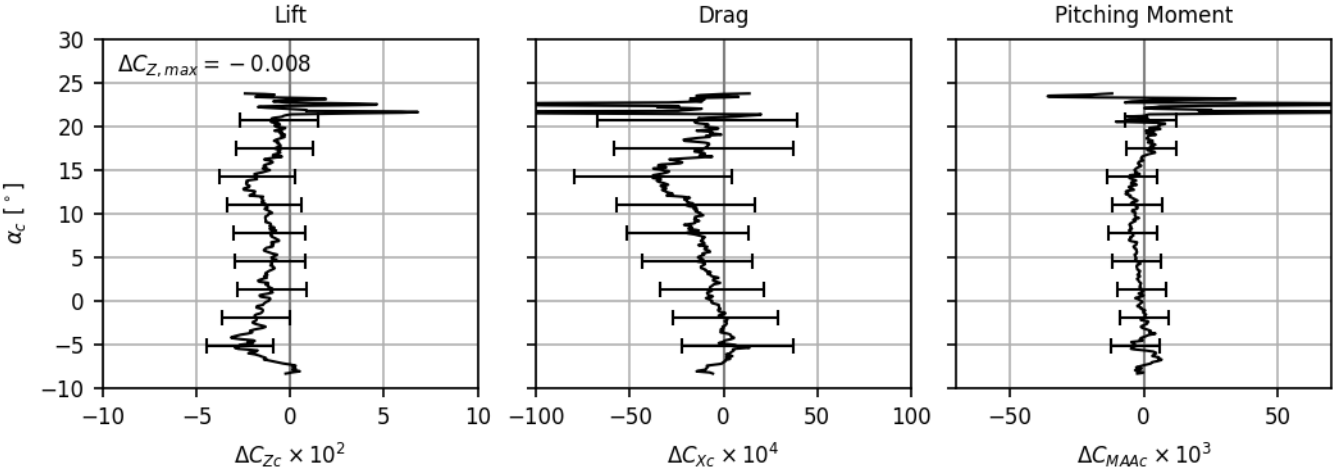

Figure 14: Difference in force coefficients during 1M campaign, between runs with tufts on left wing (run 22630/1594) and run without tufts (run 22631/1614), on LDG-HV configuration, at Mach number M_{0c} = 0.20 and Reynolds number Re_{0c} = 5.9 million.

During the 1M campaign, tufts were also applied on the right wing for a couple of runs. Figure 14 examines the effect of tufts on force coefficients at high Reynolds number. There seem to be a small reduction in lift coefficient, of the order of 0.01 to 0.02. Here again, examination of rolling moment confirmed the lift loss was localized on right wing, so that lift loss should have been doubled if tufts had been applied on both wings.

V. Overview of aerodynamic results

All results presented in this paper are all fully corrected for wall (section IV.C) and support interference (section IV.D), as indicated by the subscript "c" on each quantity reported.

A. HLPW-5 test case n°2: build-up of the landing configuration, with tail plane

Following suggestion from [19] section 4.8, several configurations of the model were tested, gradually building up the LDG configuration through intermediate configurations aiming at presenting increasingly complex flow physics.

1. Longitudinal forces

Results shown in Figure 15 start with the clean wing configuration, with tail planes. The clean wing results were obtained in a different test campaign, with the clean wing model (described in III.A.1) mounted on the same support and corrected in the same way as the present high-lift model campaign, as described in section III.1. It is worth reminding this clean wing shape is the one of the high speed CRM, hence clean wing results presented here cannot be used for the HLPW-5 test case n°2.1. Data from the present campaign are then plotted, starting with the slat extended to their LDG position (curve "+ slat"). This configuration corresponds to the HLPW-5 test case n°2.2, without nacelle and with a continuous slat, as described in section III.A.2. The flaps are then extended to their LDG position (curve "+ flap"), to correspond to the test case n°2.3, again without nacelles. The nacelles and their pylon are then added to the previous configuration, but without the chine on the nacelle inner side (curve "+ nacelle"). Finally, the full LDG-HV configuration is obtained by adding the chines on the nacelles, which corresponds to the test case n°2.4.

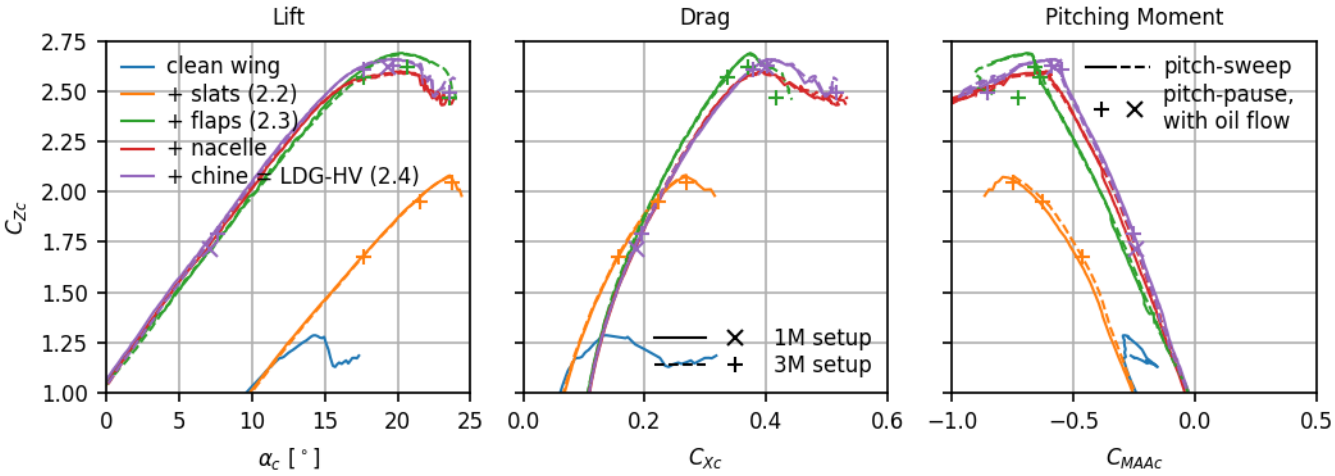

Figure 15: Longitudinal force coefficients for increasingly complex configurations, at Mach number M_{0c} = 0.20 and Reynolds number Re_{0c} = 5.9 million
(clean wing run 22319/665; high-lift runs 1M: 22638/1747, 22637/1725, 22636/1705, 22625/1387; high-lift runs 3M: 22742/1619, 22735/1533, 22731/1469, 22713/1299; high-lift runs 3M with oil flow 22743/1639, 22744/1648, 22745/1667, 22736/1548, 22737/1557, 22738/1566, 22720/1377, 22721/1386, 22722/1395, 22723/1404). Labels in between parenthesis indicate corresponding test cases in HLPW-5. Lines are pitch-sweep runs, symbols are pitch-pause runs with oil flow

2. Long term repeatability

In the Figure 15, results from both the single-strut and the three-strut test campaigns are provided. This is a good occasion to appreciate the long-term repeatability of the aerodynamic measurements in the F1 wind tunnel. As a reminder, the campaigns imply different setups, different balances and a complete disassembly of the model. The scale of the Figure 15 being not appropriate to properly see the differences in between the curves, the same data are plotted in Figure 16, as differences in force coefficients at iso-AoA.

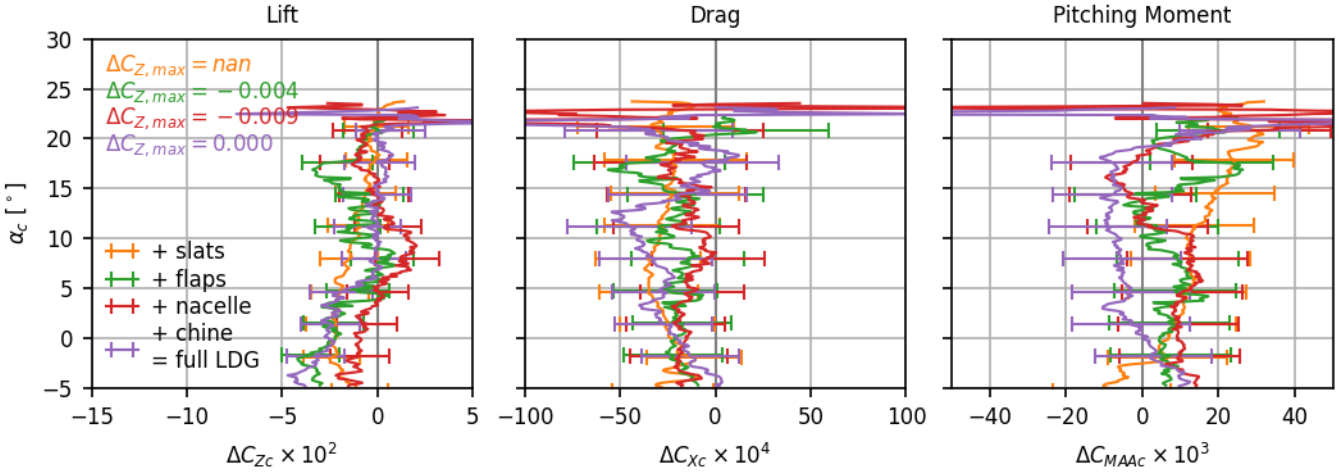

Figure 16: Difference at iso-AoA between force coefficients from 3M campaign and from 1M campaign (3M – 1M), for increasingly complex configurations, at Mach number M_{0c} = 0.20 and Reynolds number Re_{0c} = 5.9 million (run numbers, see Figure 15).

From this figure, once fully corrected for wall and support interference, repeatability in lift coefficient for all configurations, and all AoAs, mostly falls within ±0.03, and even within ±0.01 in terms of maximum lift. This result is satisfactory regarding industrial needs [4]. On average, the lift of the 3M setup is lower than the 1M setup by about 0.01, which might be linked to the penalty incurred by the tufts that were permanently installed on the left wing, see section IV.I. With the external balance, uncertainty on rolling moment is too high (see Table 6) to identify whether the left wing was actually responsible for this small lift decrease.

Repeatability in drag is within ±50 drag counts (±0.005), not as satisfactory as lift. One can note that the drag during the three-strut campaign is always lower than during the single strut campaign, by about 20 counts on average. This may be linked to the tare of three-strut support (see section IV.D) being overestimated. It is known that the drag tare is sensitive to the way the tips of the struts are handled. The strut tips are housing ball bearings to connect with the model, and these bearings are not aerodynamically shaped, as they are masked when the model is mounted on the struts. Consequently,

aerodynamic fairings are applied on strut tips when tare is performed. In doing so, there is some arbitrariness in defining the fairing size, which adds some uncertainty to the tare assessment. Generally speaking, accurate drag measurements using an external balance always pose some difficulties when it comes to properly breakdown the model drag and the part of the support that is exposed to the wind.

Overestimating the drag tare would also incur a small nose up pitching moment by about +0.005 considering the lever arm of the strut with respect to the moment reference point. This amount is too small to be spotted in pitching moment differences that show a scatter of about ±0.02, but the average is indeed on the positive side of the plot.

Most often, the discrepancies between the single-strut and the three-strut test campaigns are in line with the uncertainty estimates exposed in section IV.F.

It is worth noting that repeatability and estimated uncertainties are 5 to 10 times smaller than the typical scatter previously observed across the simulations during the HLPW-4 [3], and even better if focusing on maximum lift coefficient, so that the present dataset stands as a valuable asset for CFD validation.

3. Wing deformation

An example of wing deformation measurement is shown in Figure 17b, using nomenclature of Figure 17a. This run corresponds to a dynamic pressure of about 10 kPa, close to the highest one possible in F1, which is 14 kPa. The main aerodynamic effect of this deformation will stem from the wing twist $\delta\theta$, which reaches about −0.65° at wing tip, when lift is close to maximum. The corresponding wing tip deflection δz is 24 mm.

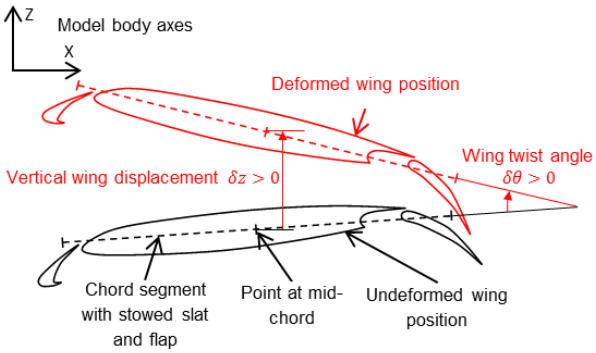

a. Schematic defining wing deformation parameters δz and $\delta\theta$.

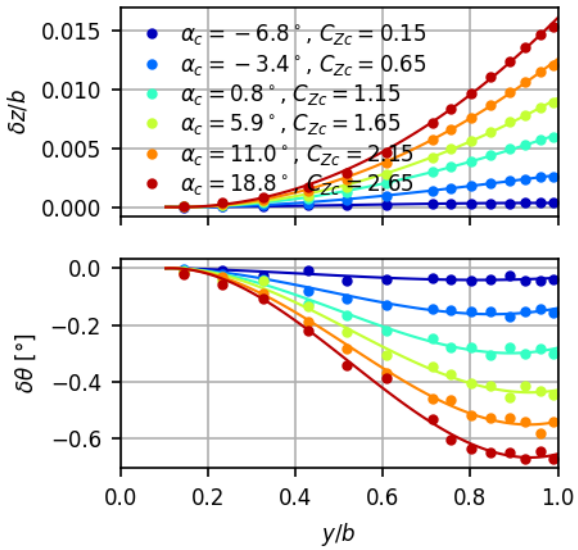

b. Measurements at Mach number M_{0c} = 0.20 and Re_{0c} = 5.9 million (run 22625/1387). Symbols: optical measurements, lines: spline interpolation.

Figure 17: Wing deformation measurement on LDG configuration.

4. Flow visualization

Flow visualizations are provided in Figure 18, Figure 19 and Figure 21. The Figure 18 compares the pictures obtained using the single-strut setup and the three-strut setup, on the LDG configuration near maximum lift. The color pattern used on the single strut was more complex, which provides a more colorful picture, but otherwise the two pictures are very similar and exhibit the same areas of flow separation, both on wing, nacelle and flaps. On the outboard wing, a wedge-shape flow separation is observed in the wake of each of the slat bracket, as was already the case in [10].

Note that there existed a small leak of blue oil during the single-strut run, indicated by the arrow in Figure 18a, which may give the illusion that there is a fifth small wedge-shaped separation near the wing tip. Closer examination of the friction lines reveals that they are not altered by the leakage, and that there is no flow separation. This benign leak was corrected afterwards, without any consequence on model forces.

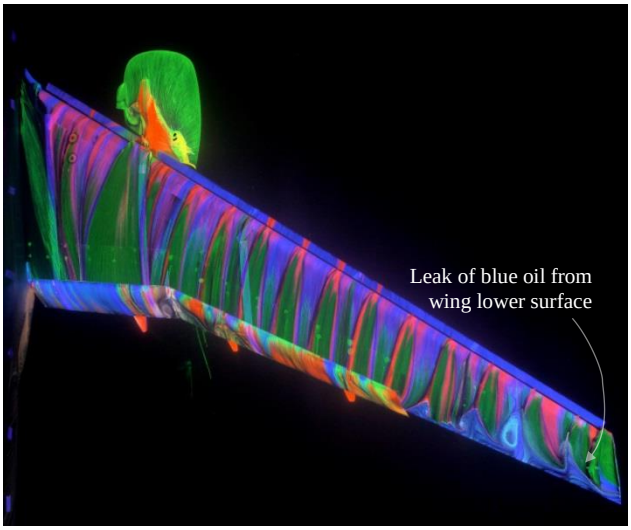

a. single-strut campaign α_c = 19.3° (run 22632/1627).

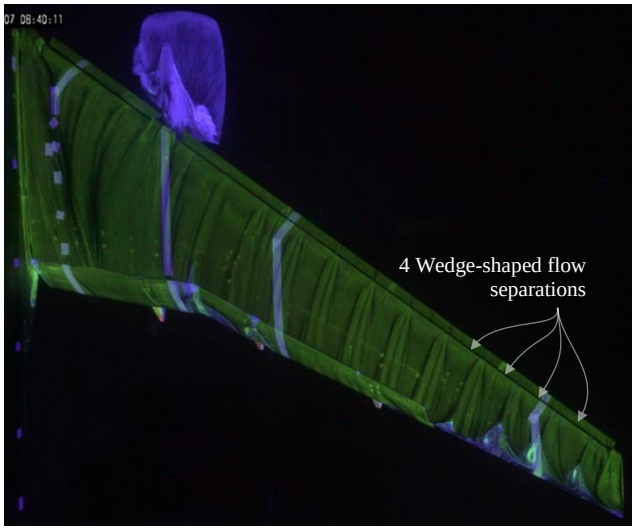

b. three-strut campaign α_c = 19.7° (run 22722/1395).

Figure 18: Oil flow visualization on LDG-HV configuration, at M_{0c} = 0.20 and Re_{0c} = 5.9 million, near maximum lift.

In Figure 19, we compare visualizations obtained using oil flow and tufts, on the LDG configuration beyond stall. The massive flow separation on the inboard wing is properly evidenced by both methods, with very similar extension. Flow separation on the outboard wing is also observed in both pictures, but it would be difficult to characterize its exact extension and topology using only the tuft technique. In both pictures, the slats are free of any separation at this AoA. Overall, the two methods provide very similar results. The oil flow technique is more accurate but is only available for a handful of AoA, whereas the tufts videos are recorded during the whole pitch-sweep.

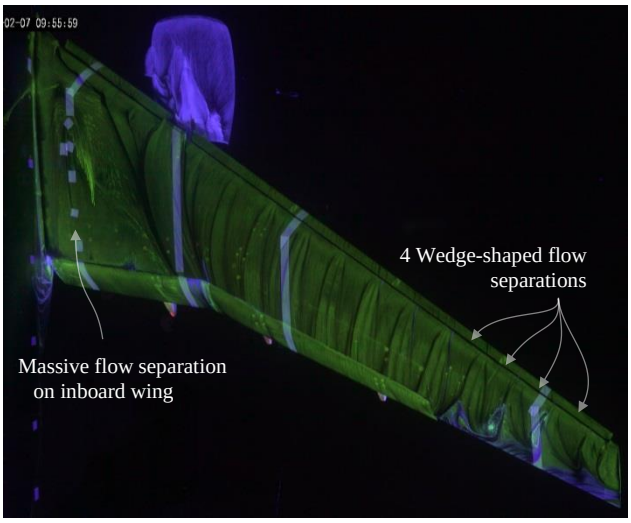

a. oil flow on right wing

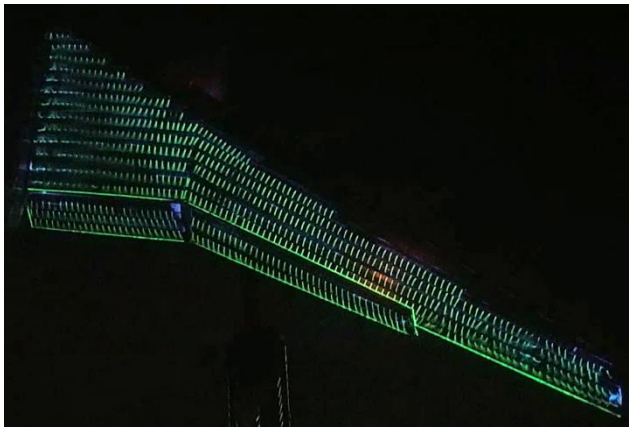

b. tufts on left wing (picture inverted)

Figure 19: Comparison of flow visualizations on LDG-HV configuration during 3M campaign, at M_{0c} = 0.20, Re_{0c} = 5.9 million, and α_c = 23.6° (run 22723/1404).

The tuft technique enabled spotting an interesting phenomenon occurring during run 22723/1404 shown in Figure 20. This run was a pitch-pause one during which the model was held at an AoA of 23.6° during about 4 min, the time required for the oil pattern to settle on the right wing. Looking at the video recording of the tufts on the left wing during this period of time, the flow on the outboard wing switches between two different states: the first state (Figure 20a) corresponds to the four wedge-shaped flow separations already identified in Figure 19a, and the second state (Figure 20b) corresponds to a massive flow separation. The shift from one state to the other seems to occur at random times, with an average switching time of the order of 1 s, i.e. a very low Strouhal number of the order of 0.005 based on L_{ref}. This random shift between two very distinct

flow states, occurring over long time scales, is reminiscent of bi-stable flow behavior such as the one identified in [36]. Further investigations would be required to further characterize this phenomenon.

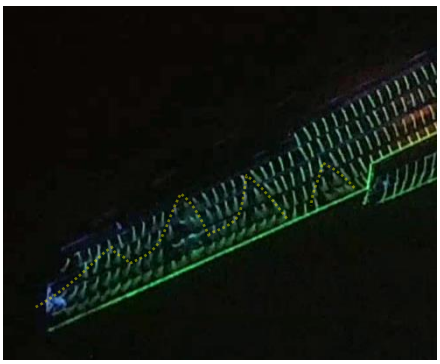

a. Wedge-shapes flow separations

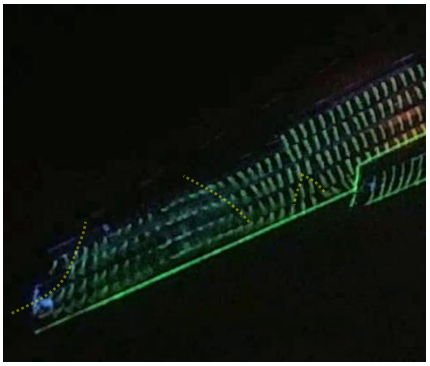

b. Massive flow separation

Figure 20: Bi-stable separation evidenced by tuft flow visualizations on LDG-HV configuration during 3M campaign, at M_{0c} = 0.20, Re_{0c} = 5.9 million, and α_c = 23.6° (run 22723/1404). Yellow dashed line were added with the help of oil flow visualization from Figure 19 to help spot the flow separations.

The Figure 21 displays oil flow visualization performed on the increasingly complex model configurations previously described. For each configuration, the figure shows the AoA corresponding to maximum lift in the left column, and an AoA past stall in the right column, with the exception of configuration WBSHV (Figure 21a and b), for which the range of AoA accessible on the three strut setup did not allow to go past stall. In depth analysis of the stall mechanism of each configuration is beyond the scope of this paper, but some comments will be made in the next section, along with examination of the wing pressure distribution.

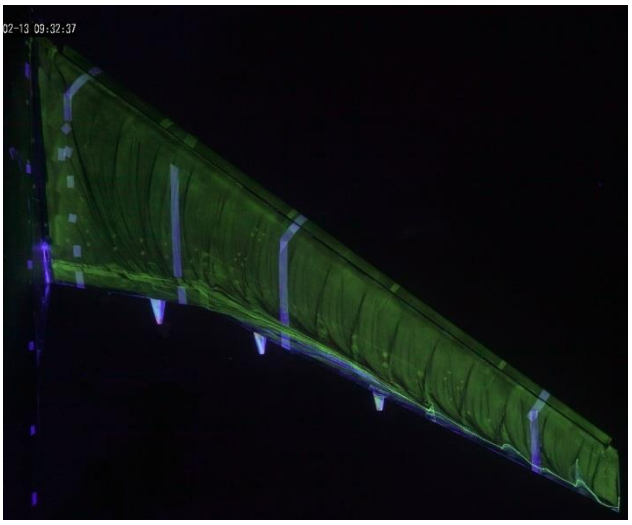

a. WBSHV configuration (case 2.2), α_c = 21.5°, C_{Zc} = 1.95 (run 22744/1648, not max lift).

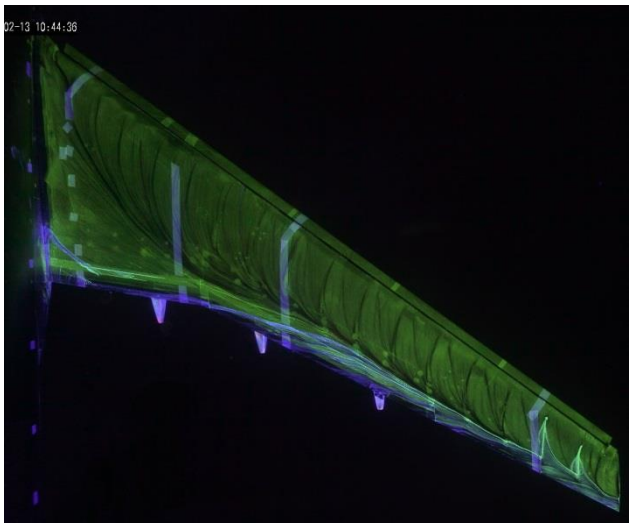

b. WBSHV configuration (case 2.2), α_c = 23.8°, C_{Zc} = 2.04 (run 22745/1667, close to max lift).

Figure 21: Oil flow visualization on various configurations, during three-strut campaign, at M_{0c} = 0.20, Re_{0c} = 5.9 million and two AoAs (left column: maximum lift, right column: post stall)

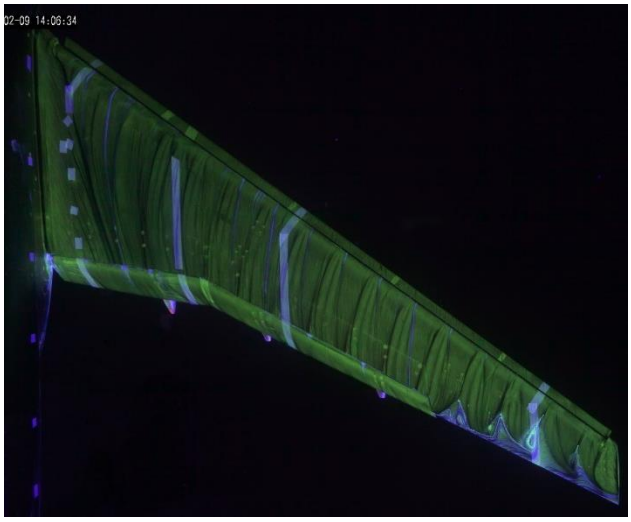

c. WBSFHV configuration (case 2.3), α_c = 20.7°, C_{Zc} = 2.62 (run 22737/1557, max lift).

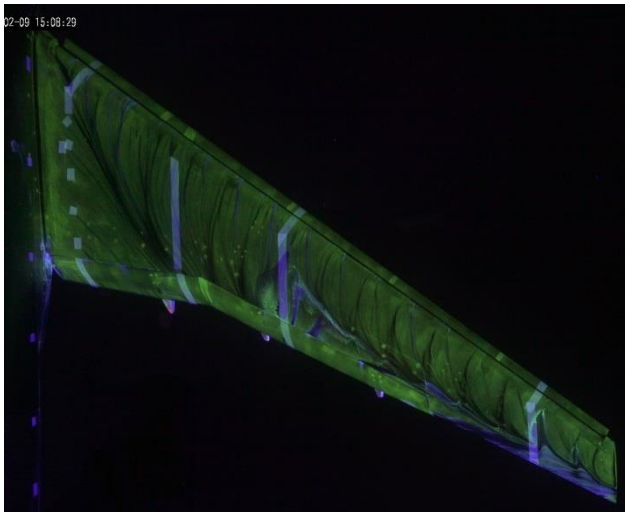

d. WBSFHV configuration (case 2.3), α_c = 23.5°, C_{Zc} = 2.47 (run 22738/1566, post-stall).

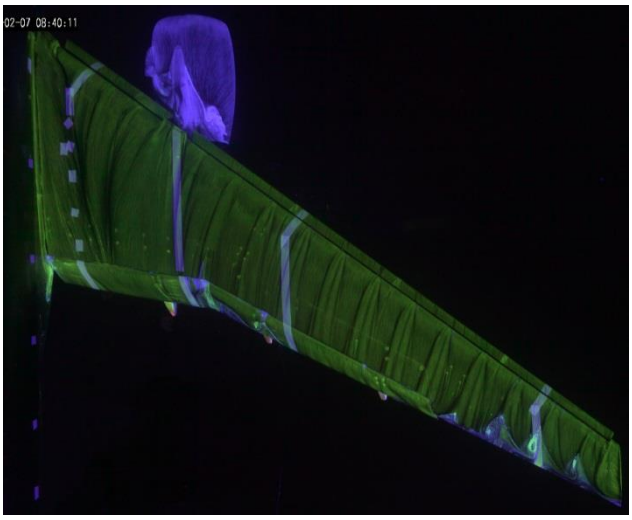

e. LDG-HV configuration (case 2.4), α_c = 19.7°, C_{Zc} = 2.63 (run 22722/1395, max lift).

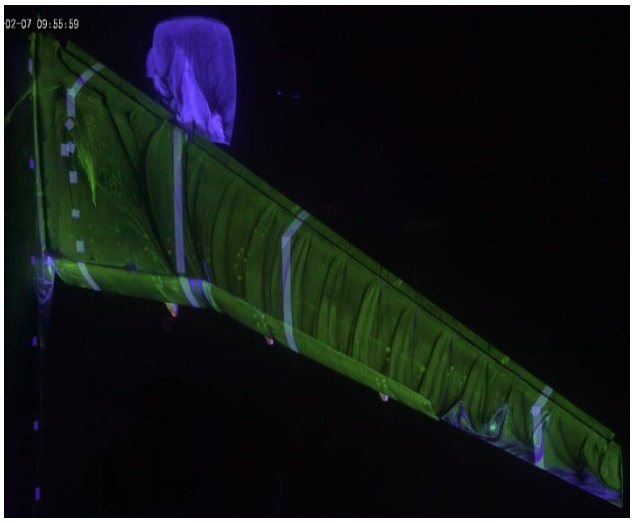

f. LDG-HV configuration (case 2.4), α_c = 23.6°, C_{Zc} = 2.50 (run 22723/1404, post-stall).

Figure 21 (concluded): Oil flow visualization on various configurations, during three-strut campaign, at M_{0c} = 0.20, Re_{0c} = 5.9 million and two AoAs (left column: maximum lift, right column: post stall)

5. Pressure distribution

The Figure 22 shows pressure distribution on the wing, from campaign on single-strut setup. The plot is organized as in [37]. The following colors and AoA are used, when data is available:

1. in black, data at an AoA of 7°, representative of normal flight conditions;
2. in green, data at an AoA about 2° to 3° before stall;
3. in blue, data at maximum lift;
4. in red, data past stall, at a point where the lift has markedly decreased.

The exact AoAs are selected to match with a run using oil flow visualization during the three-strut campaign, if such a run is available.

Some comments on stall mechanism are provided below for the three configurations.

The WBSHV configuration (HLPW-5 case 2.2) shows flow separation at the trailing edge of the wing, extending over the entire span well before maximum lift is reached. This separation is visible thanks to oil flow visualization (Figure 21a-b), but is not obvious on pressure distribution (Figure 22a). The wakes of the slat brackets tend to promote earlier trailing edge separation on the outboard wing. The lift breakdown occurs around one third of span, both on the main wing and slat.

With the flaps extended to build up configuration WBSFHV (HLPW-5 case 2.3), trailing edge flow separation on the outboard wing still exists. It is again influenced by the wake of the slat brackets to form the wedge-shaped flow separation previously discussed (Figure 21c-d). Lift breakdown is not clearly observed on the pressure distribution (Figure 22b) because the AoA range was limited to about 22° for this run. A large trailing edge flow separation is observed to take place near mid-span in Figure 21d, at an AoA of 23.5°. The flow keeps attached on the flaps up to the highest AoA investigated.

Finally, with the LDG-HV configuration (HLPW-5 case 2.4), the same kind of wedge-shaped trailing edge flow separation occurs on the outboard wing. The lift breakdown is observed to take place on the inboard wing (Figure 22c), and is also evidenced by the oil flow showing massive separation starting near the leading edge of the wing (Figure 21f). Note that the flaps show trailing edge separation at lower AoA over the whole span (from oil flow at lower AoA, not shown here). At maximum lift, this flap separation persists only near the flap junction and in the wake of the flap brackets (Figure 21f, see also Figure 27 latter in the paper), then completely disappear past stall (Figure 21f). A flow separation is also present at all AoAs on the nacelle upper surface, where it intersects the pylon.

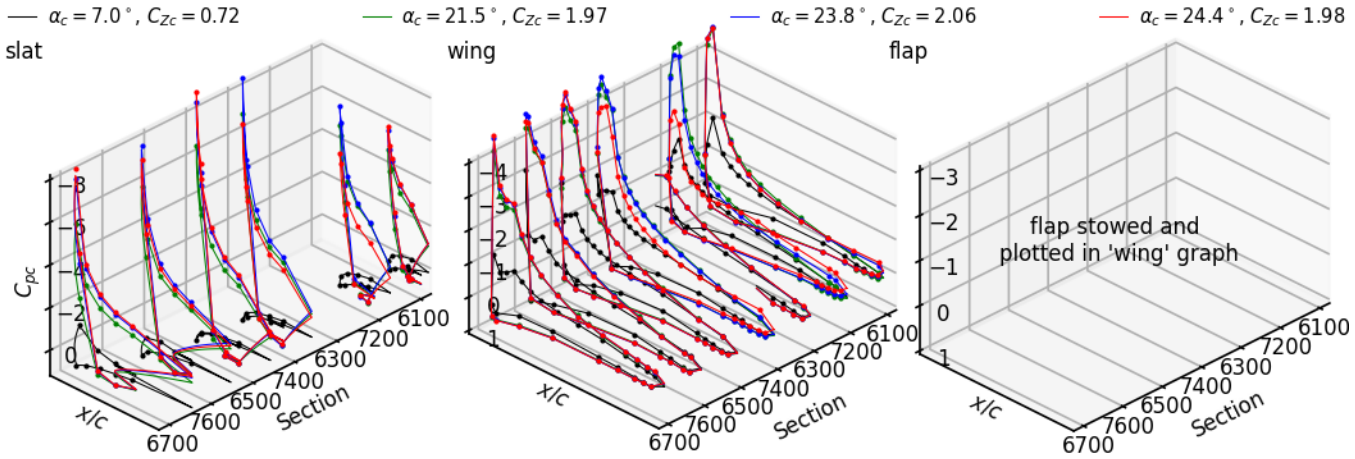

a. WBSHV configuration (case 2.2) (run 22638/1747)

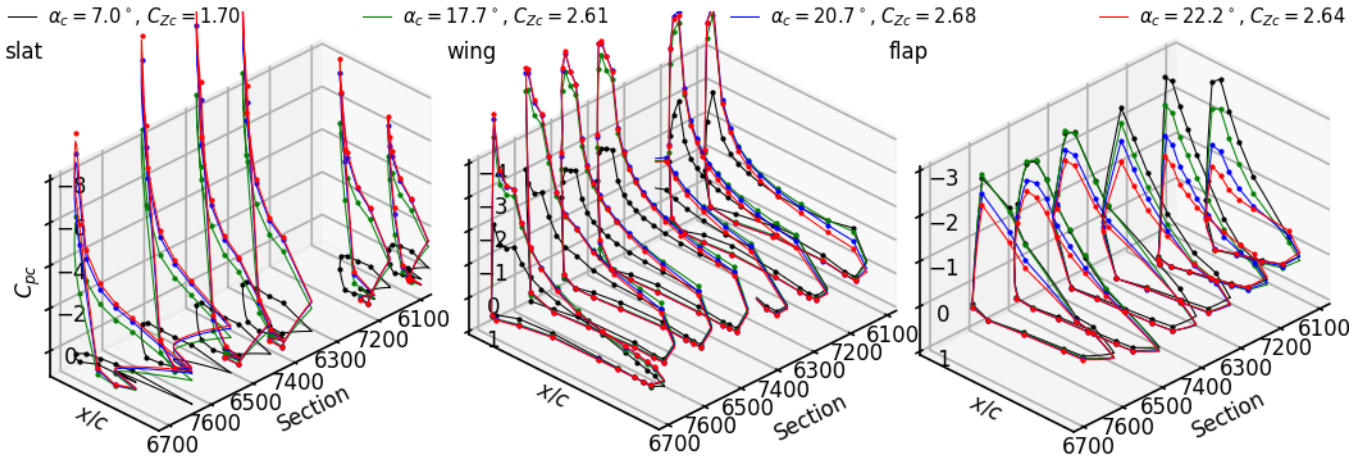

b. WBSFHV configuration (case 2.3) (run 22637/1725)

Figure 22: Wing pressure distribution on various configurations, during single-strut campaign, at M_{0c} = 0.20, Re_{0c} = 5.9 million and AoAs corresponding to flow visualization of Figure 19 (when possible); position of wing sections: see Figure 4; dots: actual measurements from pressure taps, lines: linear interpolation to ease data visualization.

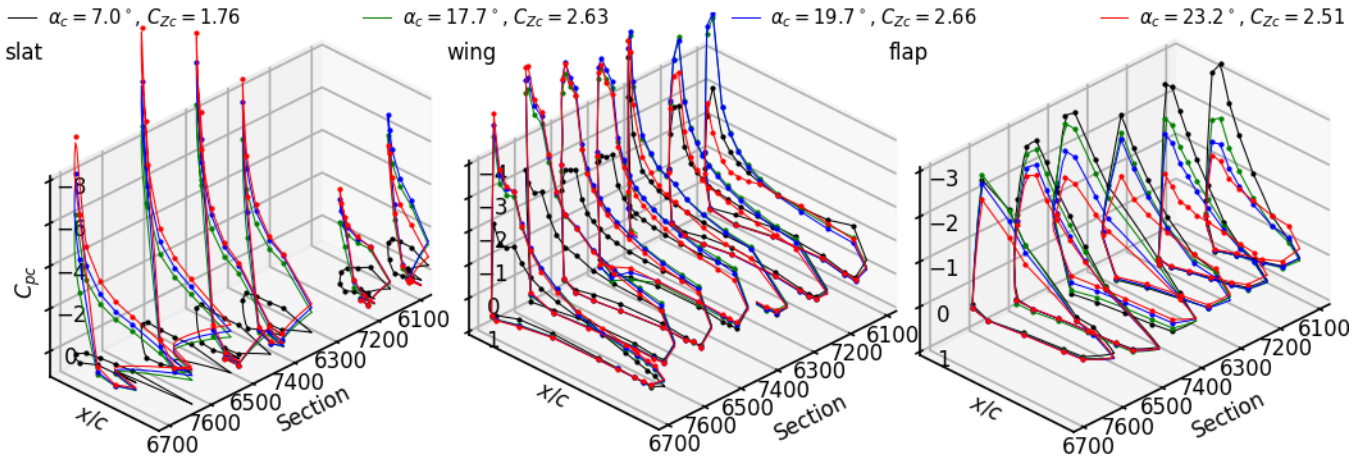

c. LDG-HV configuration (case 2.4) (run 22625/1387)

Figure 22 (concluded): Wing pressure distribution on various configurations, during single-strut campaign, at M_{0c} = 0.20, Re_{0c} = 5.9 million and AoAs corresponding to flow visualization of Figure 19 (when possible); position of wing sections: see Figure 4; dots: actual measurements from pressure taps, lines: linear interpolation to ease data visualization.

B. HLPW-5 test case n°3: Reynolds number effect on the landing configuration, without tail plane

1. Longitudinal forces

The Figure 31 shows longitudinal force coefficients of the LDG configuration, at a Mach number of 0.20 and for increasing Reynolds number from 1.5 to 5.9 million, corresponding to the wind tunnel test envelope when pressurized from 1 to 3.85 bar. As the Reynolds number increases, the maximum lift coefficient gradually increases, while the pitch-up tendency reduces. Lift-to-drag ratio also grows with Reynolds number.

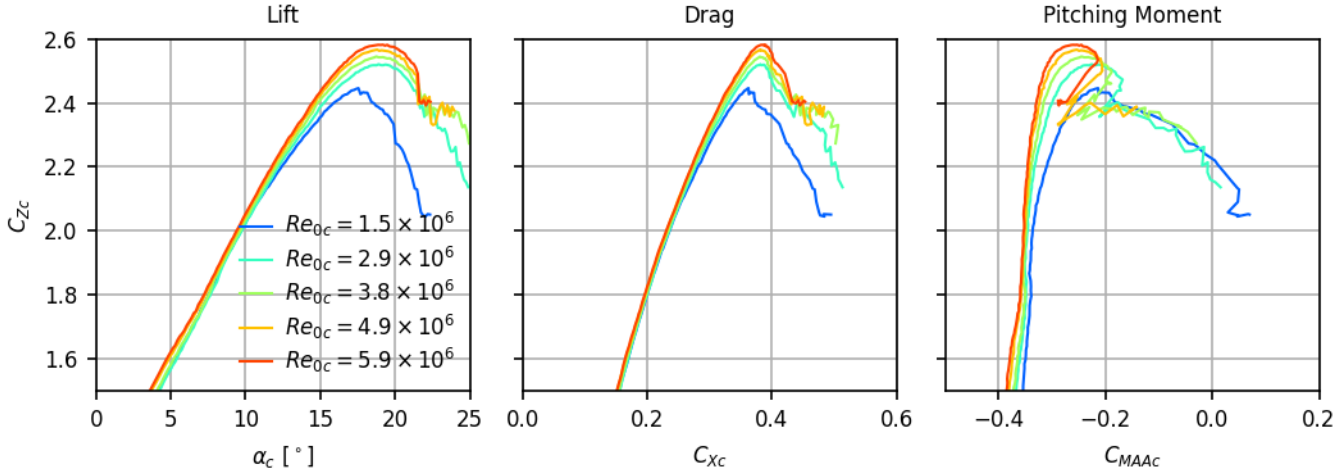

Figure 23: Longitudinal force coefficients of the LDG configuration (without tail planes), during 1M campaign, at Mach number M_{0c} = 0.20 and increasing Reynolds number Re_{0c} (runs 22642/1943, 22641/1901, 22641/1887, 22641/1871, 22640/1814).

The wind tunnel pressurization enables varying the Mach number and the Reynolds number independently. Figure 24a displays the various flow conditions performed on this model configuration, each dot being a pitch-sweep run, colored by the maximum lift coefficient $C_{zc,\max}$ achieved. The light grey triangular shape is the operating envelope of the F1 wind tunnel. The same data are plotted in a different way in Figure 24b to show Reynolds number and Mach number effects separately. Dots are actual data from the wind tunnel runs, and lines are interpolation (based on Radial Basis Function) of all the runs shown in Figure 24a. As in most situations, the maximum lift coefficient increases with Reynolds number, for reasons detailed in [38] or [39]. The maximum lift coefficient did not reach a plateau in the range of Reynolds number tested, which is still far from full scale. However it evolves in an asymptotic way that helps in extrapolating to higher Reynolds numbers. Increasing the Mach number has a negligible effect up to Mach 0.2, but then causes a drop in maximum lift coefficient. This

is attributed to the peak velocity on the leading edge of the slat reaching sonic conditions, see section V.E. Interestingly, very similar trends were reported for the Airbus A300 some 43 years ago [29].

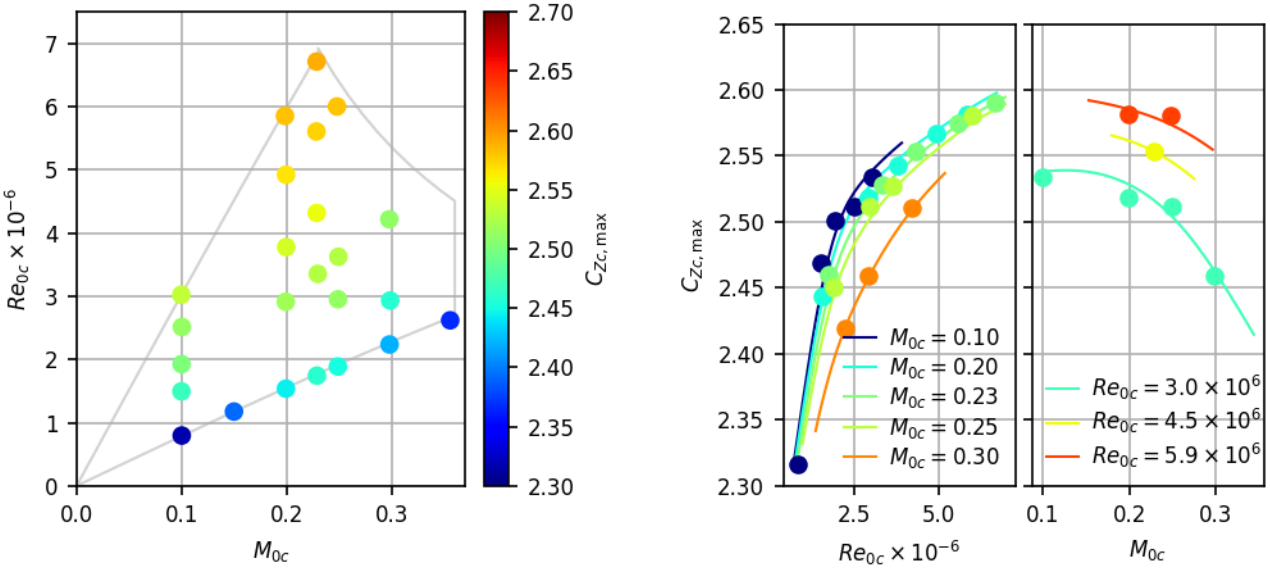

a. Combined effect in tunnel operating envelope **b. Segregated effect**

Figure 24: Effect of Mach and Reynolds numbers on maximum lift coefficient for the LDG configuration.

When performing runs by increasing tunnel velocity but under a constant total pressure, the competing effects of viscosity and compressibility, embodied in the Reynolds and Mach numbers, are involved simultaneously. In such a case, as illustrated in Figure 25, neither the Mach number nor the Reynolds number effect can be distinguished. Using only such results obtained in a constant pressure wind tunnel (e.g. atmospheric, i.e. curve p_{i0} = 1 bar in Figure 25), it would very difficult to propose any extrapolation to higher Reynolds numbers [40]. To be fair to atmospheric wind tunnel testing, it should however be reminded that the boundary layer on most of the model wing was non-transitioned in the present case. There might be a way to force boundary layer transition at low Reynolds number that brings the results closer to higher Reynolds number.

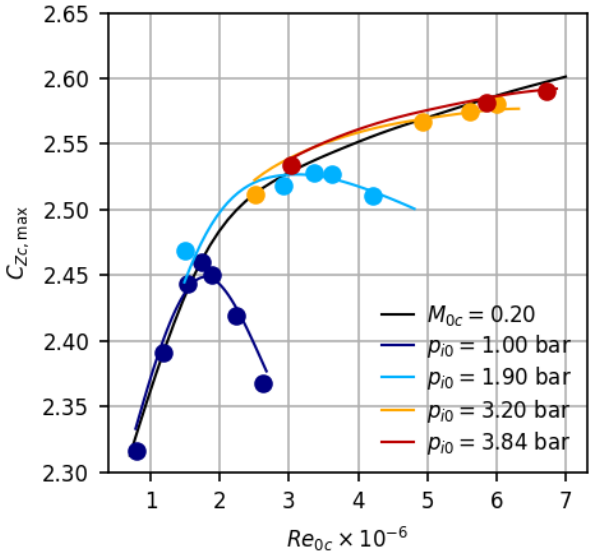

Figure 25: Evolution of maximum lift coefficient on LDG configuration, when increasing both Mach and Reynolds numbers at constant pressure (colored curves), or when increasing Reynolds number at constant Mach number (black curve).

2. Flow visualization

Flow visualization with oil flow technique (see section IV.H) were performed during the three-strut campaign, but only on the LDG-HV configuration, i.e. with the tail planes mounted. However, examination of the wing pressure distribution and the tufts visualizations reveal that the wing flow is practically identical for a given corrected AoA, whether tail planes are

mounted or not. These visualizations can then be used as validation material for the test case n°3, even if the case is without tail planes.

The Figure 26 and Figure 27 display an overview of the available flow visualizations. They were carried out at the lowest and the highest Reynolds number achieved during the experiment, and at several growing AoA.

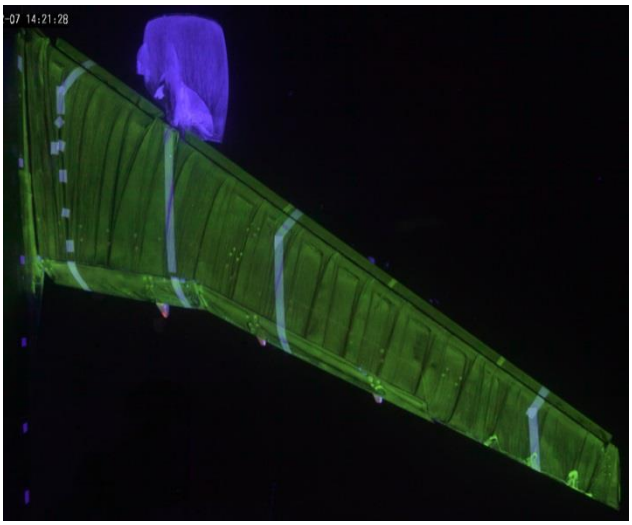

a. Re_{0c} = 1.6 million, α_c = 7.5°, C_{Zc} = 1.75 (run 22724/1413).

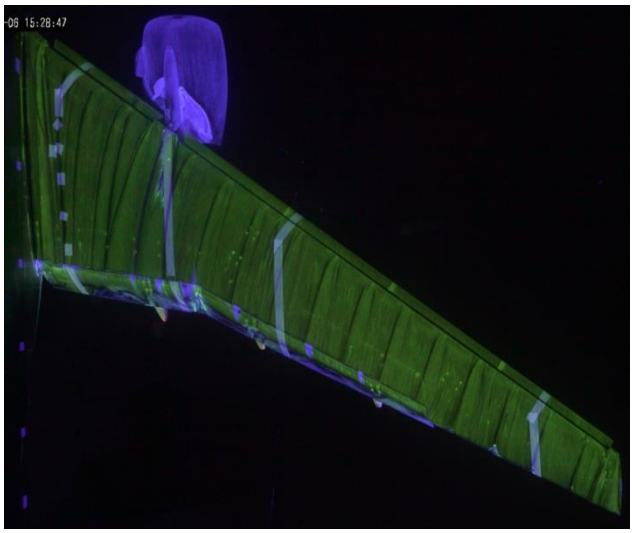

e. Re_{0c} = 5.9 million, α_c = 7.6°, C_{Zc} = 1.79 (run 22720/1377).

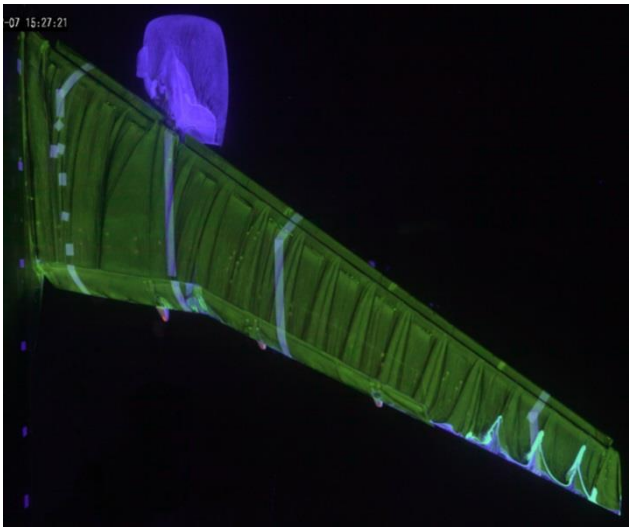

b. Re_{0c} = 1.6 million, α_c = 15.5°, C_{Zc} = 2.41 (run 22725/1422).

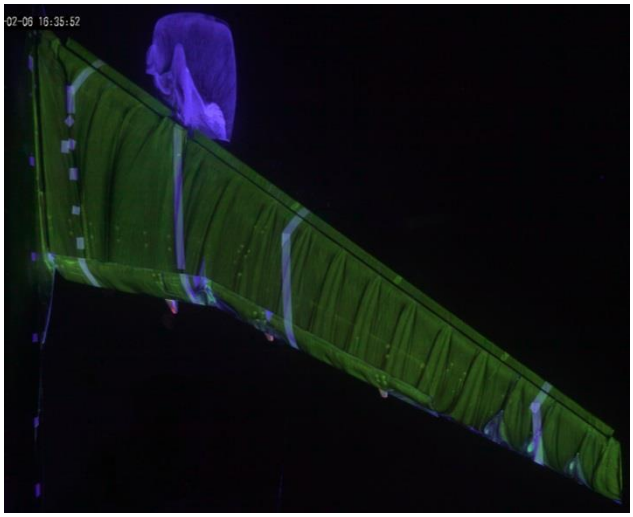

f. Re_{0c} = 5.9 million, α_c = 17.7°, C_{Zc} = 2.61 (run 22721/1386).

Figure 26: Oil flow visualization on LDG-HV configuration, during three-strut campaign, at M_{0c} = 0.20, Re_{0c} = 1.6 million (a-d) or 5.9 million (e-h) and various AoA (rows)

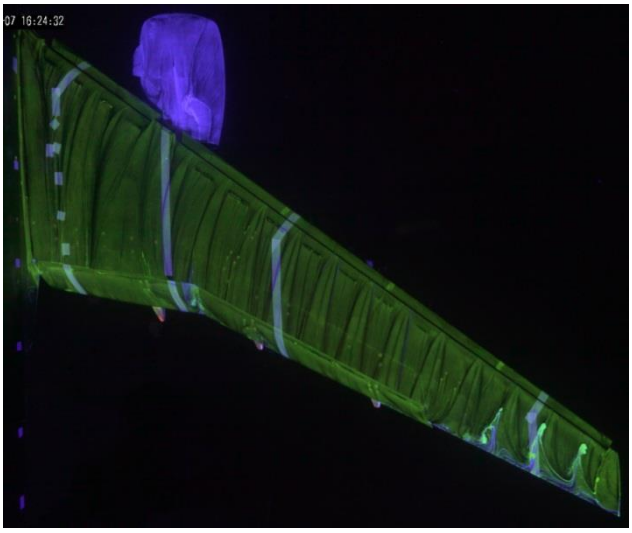

c. Re_{0c} = 1.6 million, α_c = 17.6°, C_{Zc} = 2.45 (run 22726/1433).

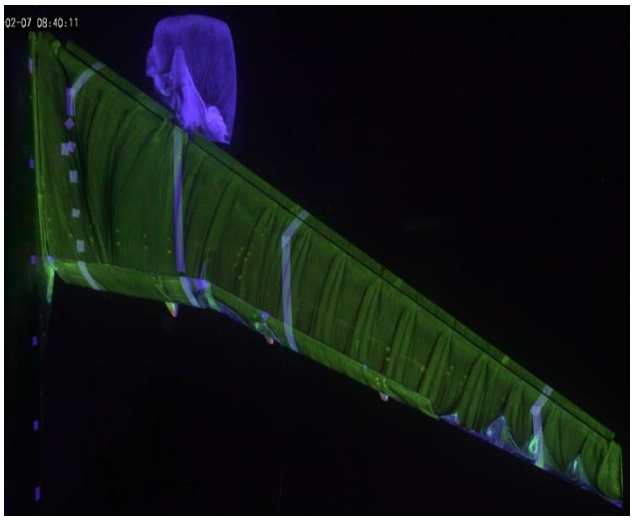

g. Re_{0c} = 5.9 million, α_c = 19.7°, C_{Zc} = 2.63 (run 22722/1395).

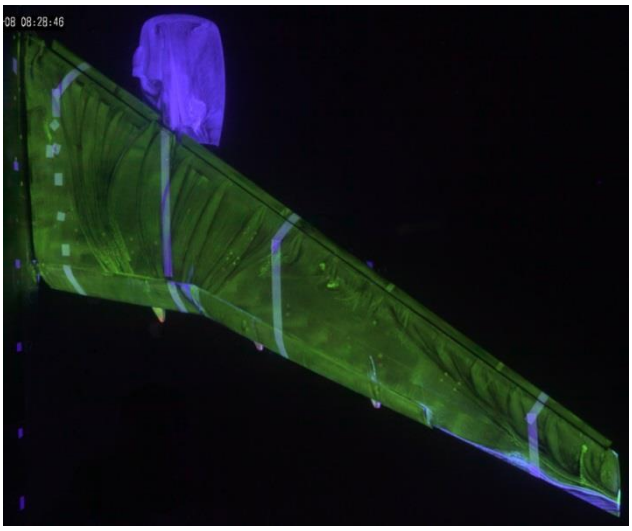

d. Re_{0c} = 1.6 million, α_c = 23.4°, C_{Zc} = 2.14 (run 22727/1440).

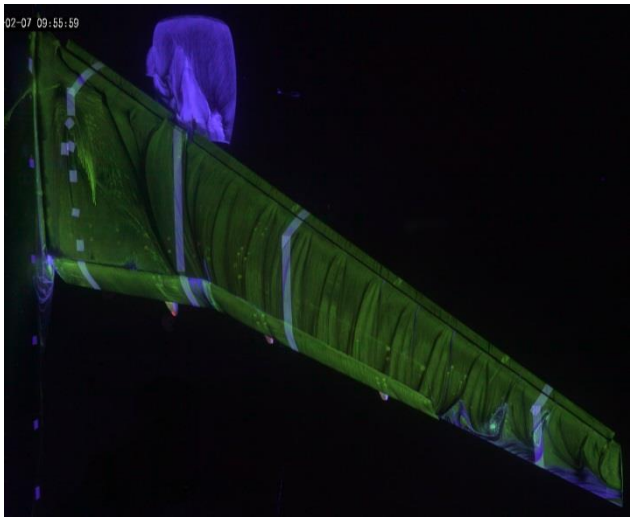

h. Re_{0c} = 5.9 million, α_c = 23.6°, C_{Zc} = 2.50 (run 22723/1404).

Figure 26 (concluded) : Oil flow visualization on LDG-HV configuration, during three-strut campaign, at M_{0c} = 0.20, Re_{0c} = 1.6 million (a-d) or 5.9 million (e-h) and various AoA (rows)

At the lowest Reynolds number, laminar separation bubbles are visible at all AoA, on the wing and on the flaps. The burst of these laminar bubbles may be responsible for the huge difference in flow physics past stall, compare Figure 26d and h.

As previously exposed, flow separation exists at the trailing edge of the flaps at low AoA, at both Reynolds number. This separation is less visible in Figure 26a than in Figure 26e because the blue oil from the flap lower side was less efficiently entrained to the upper side due to reduced dynamic pressure at the lower Reynolds number, but nevertheless is clearly visible in close-up pictures (not shown here). This flap separation persists only near the flap junction and in the wake of the flap brackets at higher AoA, with a topology that is similar at both Reynolds numbers.

Wedge-shaped trailing edge flow separation is observed on the outboard wing with similar size and shape at both Reynolds numbers.

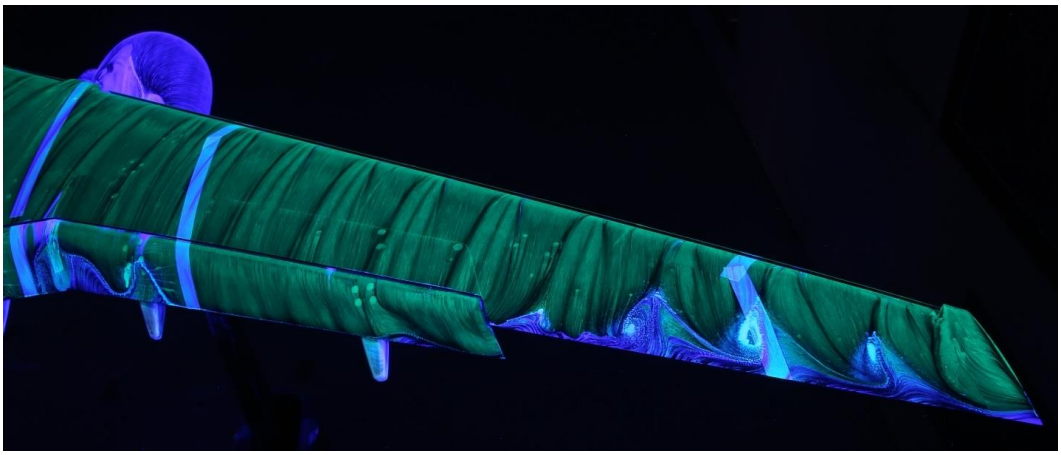

Figure 27: Oil flow visualization (close-up on outboard wing) on LDG-HV configuration, during three-strut campaign, at M_{0c} = 0.20, Re_{0c} = 5.9 million and α_c = 19.7° (C_{Zc} = 2.63).

3. Pressure distribution

The Figure 28 presents wing pressure distribution at maximum lift for each of the Reynolds number tested. It can be observed that the flow with higher Reynolds numbers can sustain more peaky pressure distribution, especially on the slat, hence increasing the load on all airfoil elements.

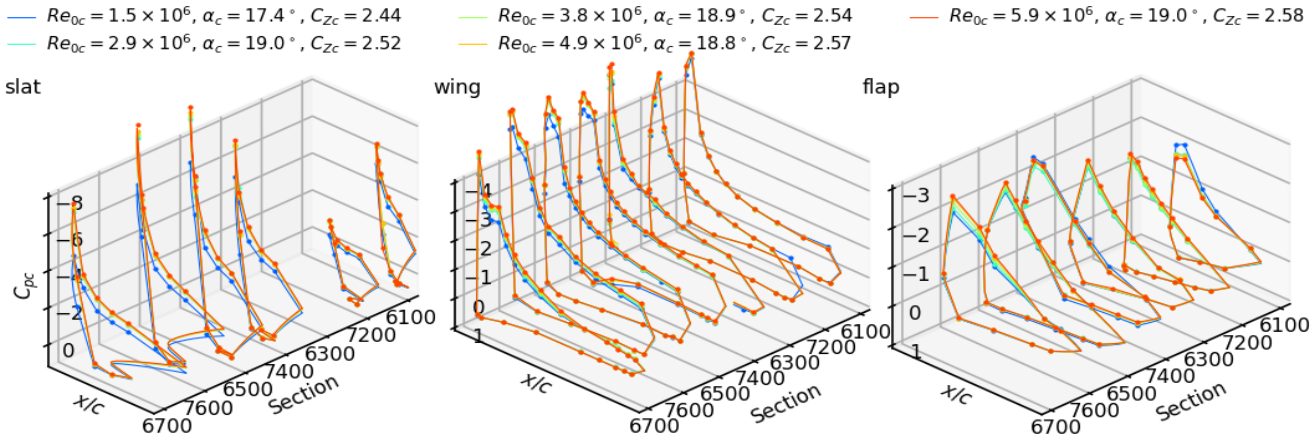

Figure 28: Pressure coefficient on wing sections, on LDG configuration, during single-strut campaign, at M_{0c} = 0.20, at various Reynolds numbers, and at maximum lift (runs 22642/1943, 22641/1901, 22641/1887, 22641/1871, 22640/1814); dots: actual measurements from pressure taps, lines: linear interpolation to ease data visualization.

The Figure 29, proposes a different perspective on this pressure data, to help in better understanding the roles of Reynolds and Mach numbers on maximum lift. In this figure, each dot comes from a pitch-sweep run, and presents the minimum pressure coefficient $C_{p,\min}$ observed on the model at stall, as a function of Mach number. Stall is here defined as the point of maximum lift $C_{zc,\max}$, except in some runs with the clean wing configuration, for which the lift never reaches a maximum but tends to level off. In that case, stall is defined as the point where the drag suddenly increases and the lift slope strongly decreases. At low Reynolds numbers (blue dots), the thick boundary layer cannot withstand a strong recompression so that the peak suction $C_{p,\min}$ is limited by the occurrence of flow separation, and therefore the maximum local Mach number remains small. In that case, flow separation is possibly influenced by laminar areas. As the Reynolds number Re_{0c} increases (yellow to red dots), higher peak velocity can be reached, typically with $C_{p,\min}$ of the order of −10 to −13, which corresponds to roughly 4 to 5 times the upstream velocity. But when the upstream Mach number M_{0c} increases above about 0.20 – 0.23, these high peak velocities locally become supersonic. Transonic phenomena, including the likely occurrence of shock waves and shock-induced flow separation, then start to negatively influence the maximum lift and pose limit values of $C_{p,\min}$. With the help of Figure 29, one can quickly understand how the flow physics at stall on this model can be different at M_{0c} = 0.20 ($C_{p,\min} \approx -13$ on the model, corresponding to a maximum local Mach number of 0.86) *vs* at M_{0c} = 0.30 ($C_{p,\min} \approx -9$ on the model, corresponding to a local maximum Mach number of 1.2). Similar trends and conclusions were exposed in [41], both

for 2D airfoils and for 3D models, and they were successfully compared to flight test data. This figure also shows that this model, when tested at a total pressure p_{i0} of 1 to 2 bar, is unable to develop its full potential in terms on lift generation, as the peak velocity is limited by insufficient Reynolds number.

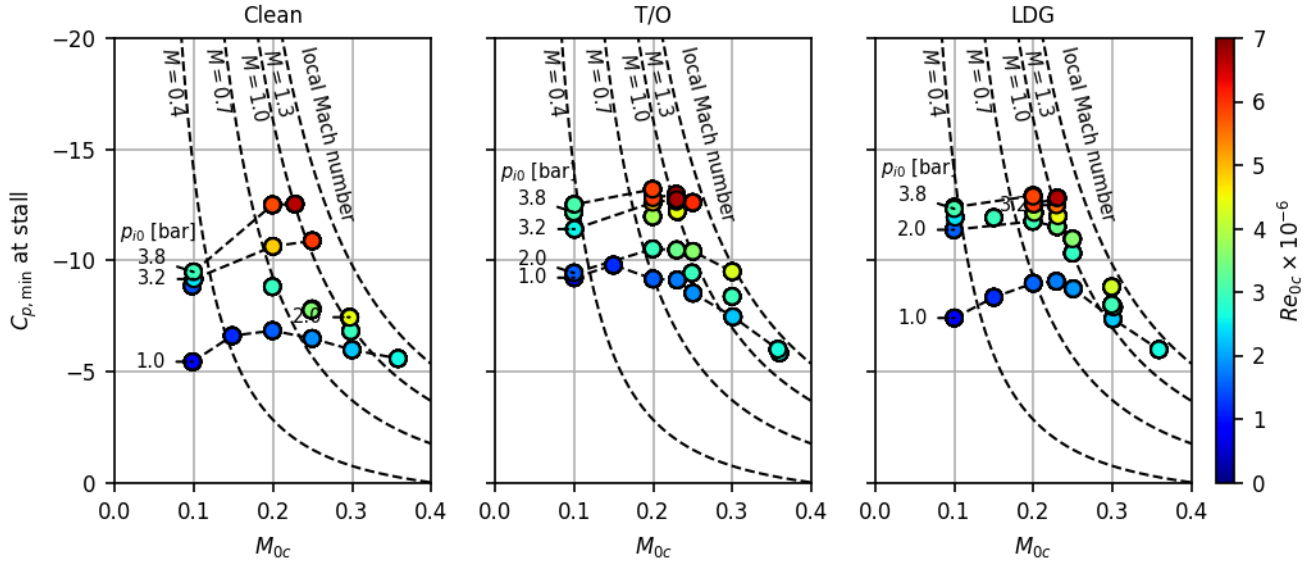

Figure 29: Minimum pressure coefficient observed across all taps of the model, at AoA corresponding to maximum lift point, as a function of Mach and Reynolds numbers, for clean, T/O and LDG configurations; straight dashed lines indicate the total pressure p_{i0} of the different runs, and curved dash lines indicate the local Mach number corresponding to the pressure coefficient.

C. Lateral characteristics

One way to identify the lateral behavior of the aircraft is to perform sweeps in sideslip angles, which is shown in Figure 30 for three different AoAs. The trend is as expected with symmetrical evolution in sideslip for the longitudinal forces (on the left), and asymmetrical for the lateral forces (on the right). Dots correspond to data taken from the AoA-sweep runs, when they "cross" the AoS-sweep runs.

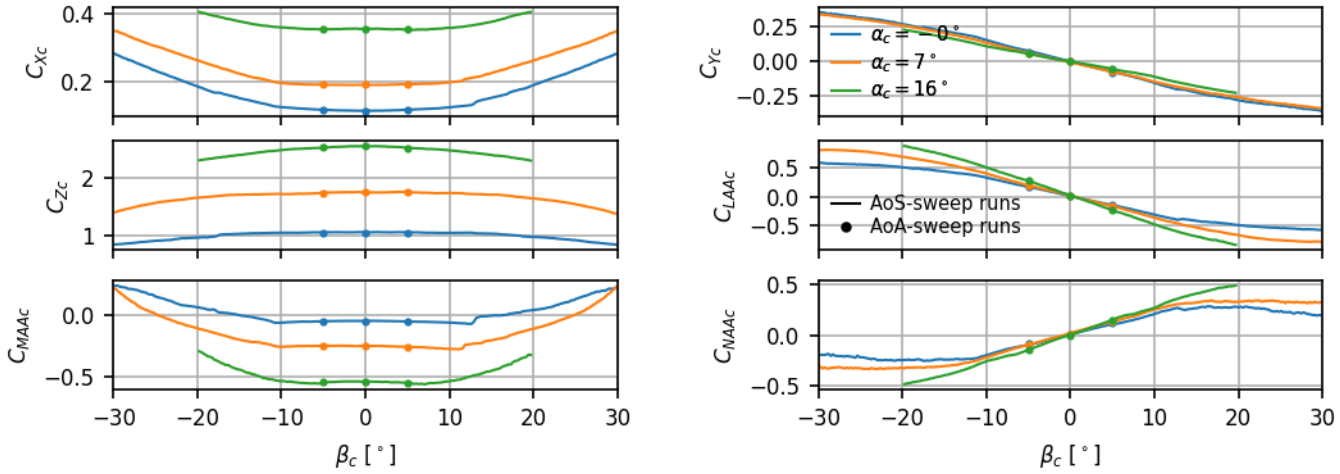

Figure 30: Force coefficients for AoS-sweep runs at different AoA on the LDG-HV configuration at Mach number M_{0c} = 0.20 and Re_{0c} = 5.9 million (solid lines: AoS-sweep runs 22625/1390, 22625/1393, 22625/1396; dots: AoA-sweep runs 22625/1387, 22625/1403, 22625/1405).

Another way to look at lateral performance is to perform pitch-sweep runs at fixed sideslip angle, resulting in data presented in Figure 31. Focusing first on the run at β = 0°, this plot shows that the smooth maximum lift point is reached without any noticeable asymmetry in forces. This is no longer the case when progressing farther into stall: at about 2° beyond maximum lift point, the lift of the left wing drops first, causing negative rolling moment and positive yawing moment. Then, at about 3° beyond maximum lift point, the lift of the right wing drops as well, and brings lateral forces back to zero. At

$\alpha_c \lesssim 15°$, small positive rolling and yawing moments exist. They are connected to the inner right wing generating less lift during this run, as already reported in section IV.G.

Looking now at the runs where a small AoS $\beta = \pm 5°$ was introduced, it is interesting to observe that the maximum lift coefficient is only slightly reduced and occurs about 1° earlier, compared with the runs at $\beta = 0°$.

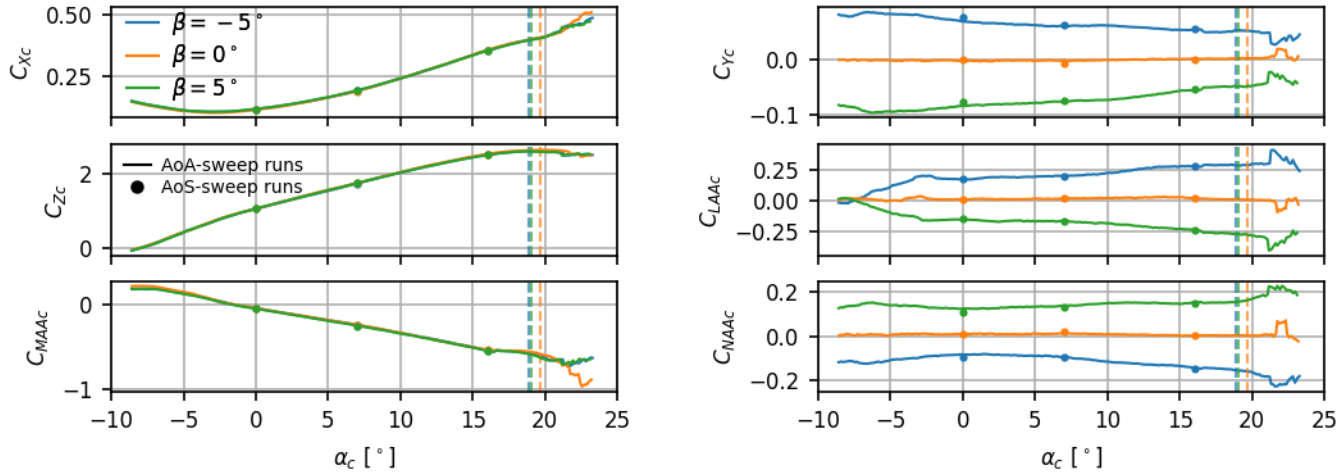

Figure 31: Force coefficients for pitch-sweep runs at different small AoS on the LDG-HV configuration at Mach number M_{0c} = 0.20 and Re_{0c} = 5.9 million (solid lines: AoA-sweep runs 22625/1387, 22625/1403, 22625/1405; dots: AoS-sweep runs 22625/1390, 22625/1393, 22625/1396; dashed lines: α_c at maximum lift coefficient).

Data from Figure 31 can be used to evaluate the lateral force derivatives by performing a second-order finite difference calculation with respect to the AoS β, e.g.:

$$\left(\frac{\partial C_{NAc}}{\partial \beta}\right)_{\beta=0°} = \frac{C_{NAc}(\beta = 5°) - C_{NAc}(\beta = -5°)}{10°}$$

Another way to calculate lateral force derivatives is to examine the slope of the curves at $\beta = 0°$ in Figure 30, by performing a linear regression of force coefficients as a function of β in the range $-5° < \beta < +5°$. The result of these calculations is shown in Figure 32.

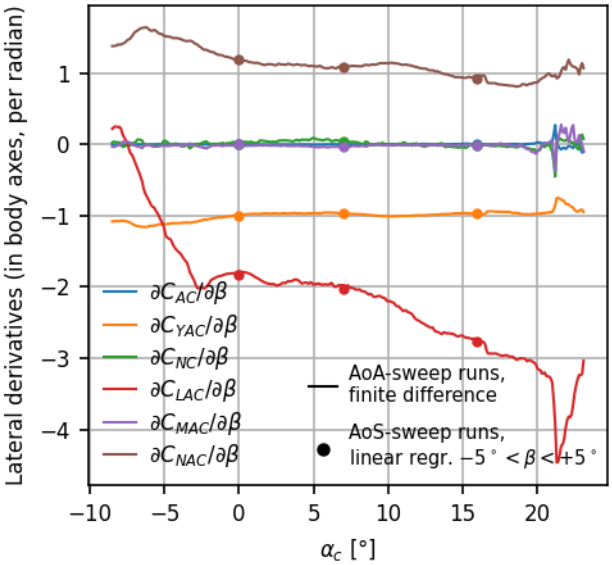

Figure 32: Lateral derivatives of force coefficients on the LDG-HV configuration at Mach number M_{0c} = 0.20 and Re_{0c} = 5.9 million (solid lines: from finite difference across AoA-sweep runs 22625/1403, 22625/1405; dots: from linear regression of AoS-sweep runs 22625/1390, 22625/1393, 22625/1396).

D. Flap setting effect, without tail planes

After another suggestion from [19] section 4.7, two off-nominal deflections of the flaps were tested. The first one here called LDG-3 has a flap deflection angle reduced by 3° compared to the reference LDG configuration, and the other one called LDG+3 has a flap deflection angle increased by 3°. As a reminder, nominal flap deflection angles are 40° for the

inboard flap and 37° for the outboard flap. These configurations were tested with no rear empennages, and at different Reynolds numbers. Results are reported in Figure 33. The more aggressive setting LDG+3 shows the largest maximum lift coefficient, at the expense of a larger drag at lower AoAs. A pitch-up is observed at stall for all configurations, but it arises earlier for the LDG−3 configuration. The ranking of the settings in terms of maximum lift coefficient and drag stays the same at low and high Reynolds number, which is not always the case.

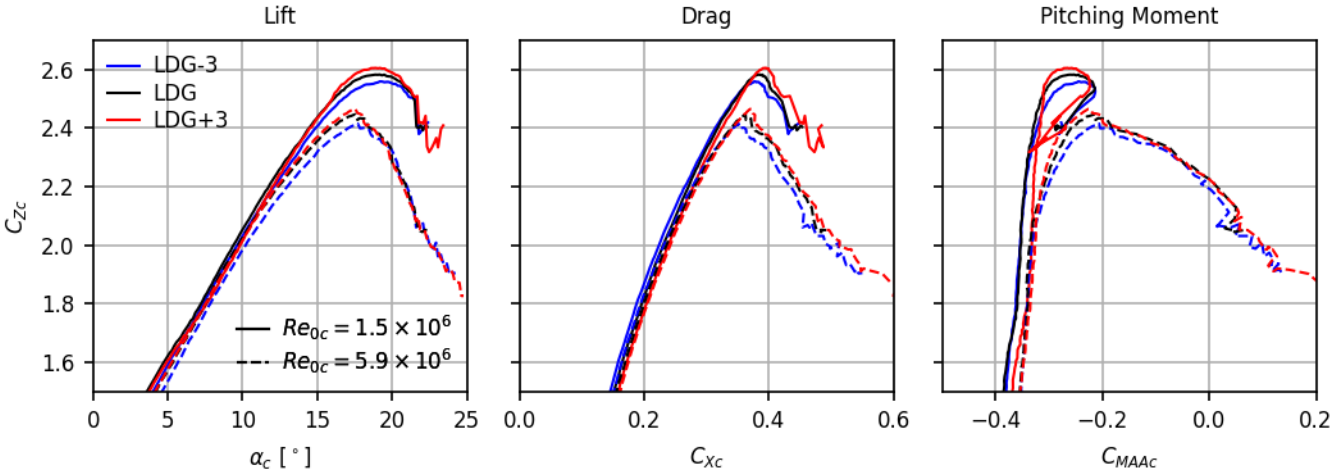

Figure 33: Flap deflection effect on LDG configuration, at Mach number M_{0c} = 0.20 and Reynolds number Re_{0c} = 1.5 million (dashed lines, runs 22644/2113, 22642/1943, 22646/2211) and Re_{0c} = 5.9 million (solid lines, runs 2055, 1814, 2131).

E. Sensitivity to model finish

As explained in section III.E, some variations in model finish were applied to evaluate the sensitivity of the results with respect to these details. As depicted in Figure 34, they had no significant effect on the model forces.

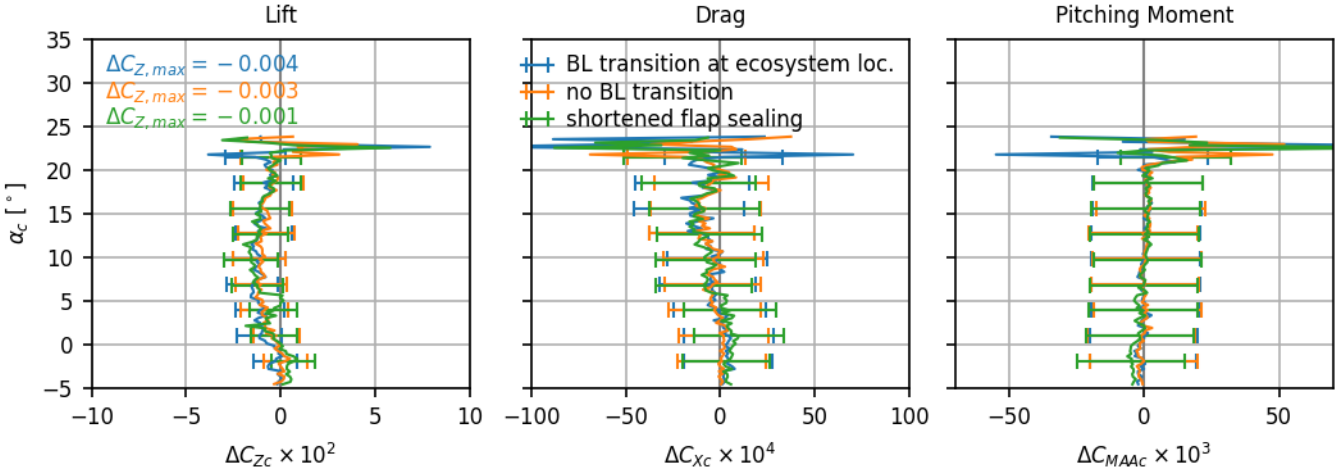

Figure 34: Effect of model finish on force coefficients, with the LDG configuration, at Mach number M_{0c} = 0.20 and Reynolds number Re_{0c} = 5.8 million: wing boundary layer transition moved downstream to reach the same location as in [10] (blue lines, run 22715/1319), no boundary layer transition on wing (orange lines, run 22714/1309), flap sealing shortened as in [10] (green lines, run 22716/1329). Reference run is 22713/1299. See section III.E for detailed description.

VI. Data sharing policy

The documentation, Computer Aided Design (CAD) shapes and dataset collected during these test campaigns is planned to be shared at different occasions, and with different partners.

In the framework of the HLPW-5, selected data have been made publicly and freely available, following the following timeline:

- January 2023 at AIAA Scitech [20]: main characteristics of the wind tunnel experiment and content of the dataset;
- March 2023: model geometry on the HLPW website [12];

- November 2023 – July 2024: partial data release on the HLPW website [12];
- August 2024 at HPLW-5 (AIAA Aviation 2024): present paper, and dataset for the official test cases of the HLPW-5 [25].

This timeline was chosen to be compatible with the HLPW-5 agenda. Indeed, this experimental database contributes to the test cases no. 2 and 3 of the workshop. Data release was first limited in order to have simulations of this configuration carried out blindly before the workshop.

The official dataset is now available on the public data warehouse hosted on recherche.data.gouv.fr, see reference [25]. A selection of data is also published on the HLPW website [12]. Beyond this public release, possible agreements and collaborations with selected partners are possible.

Data was released under a CC-BY-NC-ND license. The "NoDerivative" (ND) condition should be interpreted as forbidding alteration of the numerical data contained in the original database. Derivatives that modify the way the database is presented or formatted, or derivatives consisting in producing plots of the data, or other analyses, are permitted. Users of the database are required to give appropriate credit, which may include citing the present paper, if appropriate.

It is worth noting that this model was also recently used in the same wind-tunnel for a test including PIV measurements (unpublished data, see [20] section VI), a test in ground effect (published data, see [42]) and a test with acoustic measurements of the airframe noise (published data, see [43]).

VII. Conclusion

The main features and outcomes of the wind tunnel testing of the LRM-HL full-span model in the ONERA F1 pressurized low-speed wind tunnel have been presented. A large amount of data has already been collected during two complementary test campaigns, covering large variations in model configurations, AoA, AoS, Mach and Reynolds numbers, and including force, pressure, wing deformation, and flow visualization. The main elements of the test methodology were provided to better appreciate the quality of the database in terms of uncertainty, repeatability, and wall and support corrections.

The available dataset is expected to be very relevant as a CFD validation test case for high-lift configurations in the future, especially during the 5th High-Lift Prediction Workshop, occurring at the time of publication of this conference paper. More generally, it should be useful for the scientific community dealing with high-lift flow.

A short analysis of this database was provided, which evidenced the importance of separating Reynolds number effects from Mach number effects to be able to extrapolate wind tunnel results to actual flight conditions. Indeed, both were shown to have significant effects on performance of high-lift aircraft configuration, through very different physical phenomena. Such an analysis is enabled by the pressurization capability of a facility like the ONERA F1 wind-tunnel.

Acknowledgements

This work was funded by ONERA's research budget as part of the continual improvement of its wind-tunnel testing services. Some parts of the model were founded by a loan with the European Investment Bank. The authors would like to thank the teams in the design office, in the model workshop and in the wind tunnel for their contribution. Special thanks go to Hyacinthe Buxadera and Laurent Rossoni, who were involved as test engineers in the different campaigns carried out with this model. Laurène Dorat and Jean-Paul Desrumeaux also deserve recognition for the photographs and video recording of oil flow and tufts visualization. Several of their pictures were also used on the HLPW website, and in the Data Visualization Showcase during the conference.

References

[1] Slotnick, J., Khodadoust, A., Alonso, J., Darmofal, D., Gropp, W., Lurie, E., and Mavriplis, D., "CFD Vision 2030 Study: A Path to Revolutionary Computational Aerosciences, NASA/CR-2014-218178, March 2014. https://ntrs.nasa.gov/archive/nasa/casi.ntrs.nasa.gov/20140003093.pdf.

[2] Rumsey, C. L., Slotnick, J. P., and Sclafani, A. J., "Overview and Summary of the Third AIAA High Lift Prediction Workshop," AIAA Paper 2018-1258, January 2018. doi:10.2514/6.2018-1258

[3] Rumsey, C. L., Slotnick, J. P., and Woeber, C.D., "Fourth High-Lift Prediction/Third Geometry and Mesh Generation Workshops: Overview and Summary," *Journal of Aircraft*, Vol. 60, No. 4, July–August 2023 doi:10.2514/1.C037168

[4] Clark, A. M., Slotnick, J. P., Taylor, N., and Rumsey, C. L., "Requirements and Challenges for CFD Validation using the High-Lift Common Research Model," AIAA Paper 2020-2772, June 2020. doi: 10.2514/6.2020-2772

[5] Lacy, D. S., and Sclafani, A. J., "Development of the high lift common research model (HL-CRM): A representative high lift configuration for transonic transports," AIAA Paper 2016-0308, January 2016. doi:10.2514/6.2016-0308

[6] Rivers, M. B., "NASA Common Research Model: A History and Future Plans," AIAA Paper 2019-3725, June 2019. doi:10.2514/6.2019-3725

[7] Vassberg, J.C., DeHaan, M.A., Rivers, S.M., Wahls, R.A., "Development of a Common Research Model for Applied CFD Validation Studies," AIAA Paper 2008-6919, August 2008.
doi:10.2514/6.2008-6919
[8] Lin, J.C., Melton, L. P., Viken, S. A., Andino, M. Y., Koklu, M., Hannon, J. A., and Vatsa, V.N., "High Lift Common Research Model for Wind Tunnel Testing: An Active Flow Control Perspective," AIAA Paper 2017-0319, January 2017.
doi:10.2514/6.2017-0319
[9] Lin, J.C., Melton, L. P., Hannon, J. A., Andino, M. Y., Koklu, M., Paschal, K. B., and Vatsa, V. N., "Wind Tunnel Testing of Active Flow Control on High Lift Common Research Model," AIAA Paper 2019-3723, June 2019.
doi:10.2514/6.2019-3723
[10] Evans, A., Lacy, D., Smith, I., and Rivers, M., "Test Summary of the NASA Semi-Span High-Lift Common Research Model at the QinetiQ 5-Metre Low-Speed Wind Tunnel," AIAA paper 2020-2770, June 2020.
doi:10.2514/6.2020-2770
[11] Lockard, D.P., Turner, T.L., Bahr, C.J., and Hutcheson, F.V., "Overview of Aeroacoustic Testing of the High-Lift Common Research Model," AIAA Paper 2021-2113, August 2021.
doi:10.2514/6.2021-2113
[12] AIAA High Lift Prediction Workshop: https://hiliftpw.larc.nasa.gov/, retrieved 31 May, 2022.
[13] Goc, K.A., Moin, P., and Bose, S.T., "Large Eddy Simulation of the NASA High-Lift Common Research Model, AIAA Paper 2022-1556, January 2022.
doi:10.2514/6.2022-1556
[14] Lacy, D. S., and Clark, A. M., "Definition of Initial Landing and Takeoff Reference Configurations for the High Lift Common Research Model (CRM-HL)," AIAA Paper 2020-2771, June 2020.
doi:10.2514/6.2020-2771
[15] Cartieri, A., Hue, D., Chanzy, Q., and Atinault, O., "Experimental Investigations on Common Research Model at ONERA-S1MA–Drag Prediction Workshop Numerical Results," *Journal of Aircraft,* Vol. 55, No. 4, July 2018.
doi: 10.2514/1.C034414
[16] Cartieri, A., Hue, D., "Using RANS computations to calculate support interference effects on the Common Research Model," Advanced Wind Tunnel Boundary Simulation, MP-AVT-284, NATO, 2018.
doi: 10.14339/STO-TR-AVT-284
[17] Cartieri, A., "Experimental investigations on the Common Research Model at ONERA-S2MA," Paper AIAA 2020-0779, January 2020.
doi: 10.2514/6.2020-0779
[18] Chyczewski, T.S., Lofthouse, A.J., Gea, L.-M., Cartieri, A., and Hiller, B.R., "Summary of the First AIAA Stability and Control Prediction Workshop," Paper AIAA 2022-1680, January 2022.
doi: 10.2514/6.2022-1680
[19] Clark, A.M., Slotnick, J.P., Taylor, N., and Rumsey, C.L., "Requirements and Challenges for CFD Validation within the High-Lift Common Research Model Ecosystem," AIAA Paper 2020-2772, June 2020.
doi:10.2514/6.2020-2772
[20] Mouton, S., Charpentier, G., and Lorenski, A., "Test Summary of the Full-Span High-Lift Common Research Model at the ONERA F1 Pressurized Low-Speed Wind Tunnel," AIAA Paper 2023-0823, January 2023.
doi:10.2514/6.2023-0823
[21] Carrara, J.-M., and Masson, A., "Three Years of Operation of the ONERA Pressurized Subsonic Wind Tunnel," *12th Congress of the International Council of the Aeronautical Sciences*, ICAS, Bonn, October 1980, pp. 778–792, https://hal.archives-ouvertes.fr/hal-03224252.
[22] Woodward, D.S., François, G., Taylor, N.J., "The Aerodynamic and Structural Design of the DRA 5-Metre and ONERA F1 Low-Speed Pressurised Wind Tunnels," *Aerodynamics of Wind Tunnel Circuits and their Components*, AGARD-CP-585, 1997.
[23] Hoelmer, W., Younghans, J. L., and Raynal, J.-C., "Effect of Reynolds Number on Upper Cowl Flow Separation," Journal of Aircraft, Vol. 24, No. 3, 1987, pp. 161–169.
doi:10.2514/3.45411
[24] Mouton, S., "Numerical Simulation of the Flow in the ONERA F1 Wind Tunnel," *Journal of Aircraft*, Vol. 60, No. 2, March – April 2023.
doi:10.2514/1.C036880
[25] Mouton, S., *Data package for the 5th High-Lift Prediction Workshop*, Recherche Data Gouv, July 2024.
doi:10.57745/B8VDHO
[26] Vaucheret, X., "Recent Calculation Progress on Wall Interferences in Industrial Wind Tunnels," *La Recherche Aérospatiale*, No. 3, May – June 1988, pp 45-57.
[27] Hantrais-Gervois, J.L., and Piat, J.F., "A Methodology to Derive Wind Tunnel Wall Corrections from RANS Simulations," *Advanced Wind Tunnel Boundary Simulation*, STO-MP-AVT-284, NATO/STO, March 2018.
doi:10.14339/STO-TR-AVT-284
[28] Ewald, B.F.R. (Ed.), *Wind Tunnel Wall Corrections*, AGARD-AG-336, 1998.
[29] Quémard, C., and Earnshaw, P.B., "Comparison of the results of tests on A300 aircraft in the RAE 5 metre and the ONERA F1 wind tunnels," *Aerodynamic Data Accuracy and Quality: Requirements and Capabilities in Wind Tunnel Testing*, AGARD-CP-429, July 1988.
[30] Lee, S., Broeren, A., Woodard, B.S., Lum, C.W., and Smith, T.G., "Comparison of Iced Aerodynamic Measurements on a Swept Wing from Two Wind Tunnels," AIAA Paper 2018-3493, June 2018.
doi:10.2514/6.2018-3493

[31] Saiz, M., and Quémard, C., "Airbus A310 Essais dans la soufflerie F1 de l'ONERA Comparaison vol-soufflerie," *Wind Tunnels and Testing Techniques*, AGARD-CP-348, February 1984.
[32] S. Mouton, "Numerical investigations of model support interference in subsonic and transonic wind tunnels," *8th ONERA-DLR Aerospace Symposium*, October 17-19, 2007, Göttingen, Germany. https://hal.archives-ouvertes.fr/hal-03017003v1
[33] Skinner, S.N., and Zare-Behtash, H., "Semi-span wind tunnel testing without conventional peniche," *Experiments in Fluids*, Vol. 58, November 2017. doi:10.1007/s00348-017-2442-7
[34] Yokokawa, Y., Murayama, M., Uchida, H., Tanaka, K., Ito, T., and Yamamoto, K., "Aerodynamic Influence of a Half-Span Model Installation for High-Lift Configuration Experiment," AIAA Paper 2010-684, January 2010. doi:10.2514/6.2010-684
[35] Bousquet, J. M., Lyonnet, M., and Mignosi, A., "New Measurement Techniques in the Onera Large Wind-Tunnels," 25th Congress of the International Council of the Aeronautical Sciences,Vol. 3, ICAS, Bonn, 2006, pp. 1652–1660. https://hal.archives-ouvertes.fr/hal-03224281
[36] Grandemange, M., Gohlke, M., and, Cadot, O., "Turbulent wake past a three-dimensional blunt body. Part 1. Global modes and bi-stability," *Journal of Fluid Mechanics*, Vol. 722, May 2013. doi:10.1017/jfm.2013.83
[37] Rudnik, R., "Stall Behaviour of the EUROLIFT High Lift Configurations," AIAA Paper 2008-836, January 2008. doi:10.2514/6.2008-836
[38] Smith, A.M.O., "High-Lift Aerodynamics," *Journal of Aircraft*, Vol. 12, No. 6, June 1975. doi:10.2514/3.59830
[39] Woodward, D.S., Hardy, B. C., and Ashill, P. R., "Some Types of Scale Effect in Low-Speed, High-Lift Flows," ICAS Paper 4.9.3, Jerusalem, 1988.
[40] van Dam, C.P., "The aerodynamic design of multi-element high-lift systems for transport airplanes," *Progress in Aerospace Sciences*, Vol. 38, Issue 2, February 2022. doi:10.1016/S0376-0421(02)00002-7
[41] Thibert, J.J., "The GARTEUR High Lift Research Programme", *High-Lift System Aerodynamics*, AGARD-CP-515, September 1993.
[42] Mouton, S., and Charpentier, G., "Test in Ground Effect of the High-Lift Common Research Model at the ONERA F1 Pressurized Low-Speed Wind Tunnel", to be published at AIAA Aviation 2024.
[43] Mouton, S., and Davy, R., "Aeroacoustic Testing of the High-Lift Common Research Model at the ONERA F1 Pressurized Low-Speed Wind Tunnel", to be published at AIAA Aviation 2024.